ABSTRACT

Title of Document: GAS PHASE SYNTHESIS OF ALUMINUM AND CORE-SHELL NICKEL-IRON OXIDE NANOPARTICLES

Daniel C Pines, Masters of Science, 2009

Directed By: Professor, Dr. Michael Zachariah, Department of Mechanical Engineering and Chemistry

In this master's thesis I will address the design of two aluminum and one nickel-iron oxide core-shell nanoparticle reactors, as well as the selection of the chemical precursors' triethylaluminum (TEA), aluminum trichloride, nickel carbonyl, and iron pentacarbonyl. This research provides evidence for the generation of aluminum oxide passivated aluminum nanoparticles from TEA, the failure to completely dissociate aluminum trichloride, and the successful growth of iron oxide (shell) onto nickel (core) nanoparticles. Reactions and synthesis are carried out in gas phase allowing the use of specialized aerosol sampling and characterization techniques. In addition to studying the particle in situ, TEM and EDS measurements are preformed post collection. Motivation for this work is driven by the nanoparticle's enhanced performance when used in explosive and propellants.

GAS PHASE SYNTHESIS OF ALUMINUM AND CORE-SHELL NICKEL-IRON OXIDE NANOPARTICLES

By

Daniel Corey Pines

Thesis submitted to the Faculty of the Graduate School of the
University of Maryland, College Park, in partial fulfillment
of the requirements for the degree of
Masters of Science in
Materials Science and
Engineering
2009

Advisory Committee:
Dr. Michael Zachariah, Chair
Dr. Sheryl Ehrman
Dr. Manfred Wuttig

Acknowledgment

I would like to thank my parents, brother and girlfriend for their guidance and reassurance during my studies both in under and post graduate. My research advisor for teaching me all I know about aerosols and energetic nanoparticles.

Table of Contents

List of Tables

List of Figures

Chapter 1: Introduction and Background

The field of metallic nanoparticles, particular aluminum, has attracted the attention of the military, explosive engineers and general researchers interested by the novel behavior in sub-100nm diameters. Their roles in thermite mixes to increase burn rates and as additives to conventional monomolecular high explosives, where traditionally micron or larger sized aluminum are used, provide empirical benefits. A gas phase synthesis of aluminum and nickel nanoparticles is presented in this master's work. Both electron microscopy and aerosol based instruments are employed in the investigation. The paper covers two major examinations; the attempted synthesis of aluminum nanoparticles from the precursors: triethylaluminum (TEA) and aluminum trichloride ($AlCl_3$), as well as the coating of nickel nanoparticles by an iron oxide layer in a core-shell structure.

1.1 Why Aerosol?

A quick examination into current methods being used by large scale commercial generation of nanopowders, aluminum and other metals, reveals they are dominated by aerosol processes. Aerosol/gas phase systems inherently lend themselves to industrial scale productions because they are an on-line continuous process. Liquid based processing is typically a batch procedure, where solvent use quickly becomes expensive requiring additional recycling equipment. In a research lab, the cost of solvent is usually negligible considering the amount of product being developed, but these costs grow quickly in a full scale production plant. Ideally a gas phase system will be simpler, and more easily scaled up from lab to commercial production [1].

The flow of particles, including those in the nano regime, has been long studied by the field of aerosol dynamics. Formation of aerosols and their study has applications ranging from clouds and atmospheric effects [2; 3] to the growth of carbon nanotubes[4]. This information is vital in constructing an aerosol nanoparticle reactor and modeling the physical properties of the particle distribution. Using these models and equations we can study our newly created aerosol. Even more, we can predict and tailor the interaction of two aerosols mixing. Clearly this will be very useful when attempting to grow a coating layer on our host particles.

Experimentally, we use two primary in situ instruments popular in the aerosol discipline; the differential mobility analyzer (DMA) and the condensation particle counter (CPC). When used in conjunction, the devices are referred to as a scanning mobility particle system (SMPS). From this equipment we can track relative size and number concentrations of our aerosol.

1.2 Scanning Mobility Particle System

The DMA is responsible for the size selection of the aerosol. Essentially it is an "on the fly" tunable filter, allowing only a desired particle size to flow out of the device. The theory behind the device is based on the balancing of two forces exerted on a particle; Coulombic and Stokes drag forces. In practice, an electric field is generated between two concentric metal cylinders, one placed inside the other. A charged particle is carried by the sheath flow to the electric field. Once it enters, it can either impact before, after or "on" the exit slit as seen on Figure 1-1. The balancing of the drag force, governed by particles' surface area, and the Coulombic electrostatic force, controlled by the electric

potential across the cylinders, will determine what size particles can enter the exit slit. A diagram of the fundamentals of a DMA and the actual TSI model we use are show in Figure 1-1[5].

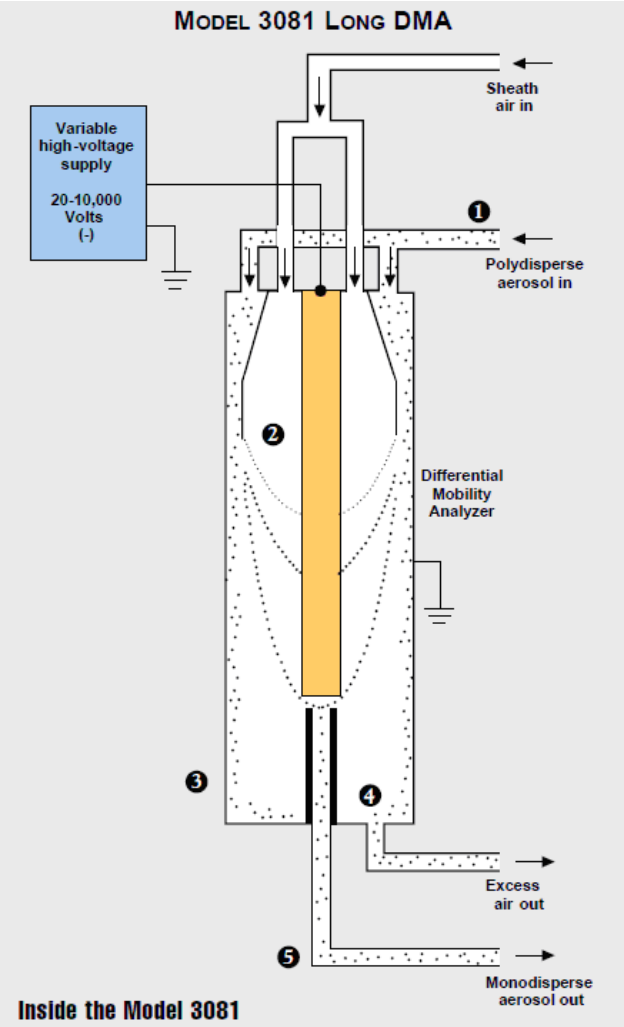

Figure 1-1: 1) charged aerosol is supplied 2) positive charged particles are attracted to center 3) negative charged particles are repelled to outer wall 4) uncharged particles are carried out unaffected 5) desired mobility size particles exit through monodisperse out[5]

An opening at the top allows the flow of aerosol to enter and the narrow slit on the inner cylinder allows the particular particle size to escape to a monodisperse flow out. The rest of the aerosol is either exhausted directly or filtered and recycled back into the

aerosol flow. If we imagine a flow of singlely charged polydisperse particles entering the device, each particle will feel a different drag force. By controlling the applied voltage across the cylinder walls, we can "impact" our particles at the exit slit and carry them out. All other particles that do not meet this physical balancing criteria will either impact before or after the narrow exit slit, flowing to a separate exhaust.

In reality the instruments selects particles based off surface area and attributes a mobility diameter to it; the less spherical a particle the greater the deviation of mobility diameter from actual diameter. When in the nano-regime, the instrument must be able adjust to account for Brownian motion of the particles, and the subsequent correction to the actual drag force imparted on the nanoparticle. This correction is known and describe in more detail in Friedlander[2].

The second half of the SMPS is the condensation particle counter. While the CPC can be used alone to calculate the concentration of our polydisperse flow, it becomes a more powerful tool when counting the size selected particles (monodisperse) flowing out of the DMA. The process works as follows; instead of selecting one applied voltage, the DMA scans through voltages over a given time span. In each time interval where the voltage is held constant for around a second, a certain size particle flows to the CPC where concentration is counted. If run over a range of voltages, analogous to particle size, one can calculate size/concentration distributions for an input polydisperse aerosol.

If large enough, particles in an aerosol can be individually counted using laser optics and total concentration can be tallied. With nanoparticles, there isn't sufficient light blocking ability to register a count. That is why before passing to the optic's chambers the particle are exposed to a warm vapor of n-butanol. The n-butanol vapor

cools and condenses on the particles surface, 'growing them up' to a laser detectable size, which in turn generates a number count for a given volume of gas[2]. It is this size and concentration that most helps typify an aerosol.

1.3 Energetics Basics

Simply, energetics are semi-stable materials that store chemically energy that can be released through oxidation in rapid reaction[6; 7]. The properties of said energetic materials depend directly on the type of fuel/oxidizer combination. Energetics generally can be divided into two categories: monomolecular high explosives and thermites/ pyrotechnics. The burn rate, or detonation velocity if reaction occurs faster than speed of sound, is often considered the figure of merit for an energetic[6; 7]. Equally as important to characterizing an energetic is the potential energy density of the compound, e.g. the amount of energy released in an idealized reaction. While a monomolecular explosive reacts faster with a larger burn rate/detonation velocity than a thermite, the energy density of most thermites exceeds that of even the most modern and powerful high explosive compound, CL-20[8]. See Figure 1-2. This has been the challenge posed to energetic researchers.

Until the last few decades, the focus has been to increase the energy density of monomolecular explosives, as it was believed the reaction chemistry of thermites had already been maximized. With the ability to produce, and integrate sub-micron size thermite powders, a new study of nanometric thermites has evolved.

1.3.1 Speed vs. Energy

In a monomolecular explosive, the atomic separation of fuel and oxidizer allows for faster reactions. The fuel and oxidizer in a traditional thermite would be macroscopically separated. Moving to nano-based thermites closes this fuel/oxide separation distance, potentially increasing burn rates while maintaining the large energy density. While one might expect the sole goal of the energetic material's field to be to maximize both these quantities, much effort has been directed to tuning these thermites, allowing the user to tailor the material for their own needs.

In the case of thermites, the fuel is a metal and the oxidizer is traditionally a metal oxide. This reaction is simple, but very effective.

$$M_{(1)}O(s) + M_{(2)}(s) \rightarrow M_{(1)}(s) + M_{(2)}O(s) + \Delta H \quad (1)$$

Equation 1 describes a typical thermite reaction, M_1O (a metal oxide) and M_2 (a metal) are chosen so that their reaction is favorable and exothermic. Energy released from these materials results from the rapid oxidation of M_2, making it the crucial ingredient when designing a potential thermite. In other words, we get a notion to the energy density of a thermite by examining the enthalpy released from an oxidation of the M_2 metal.

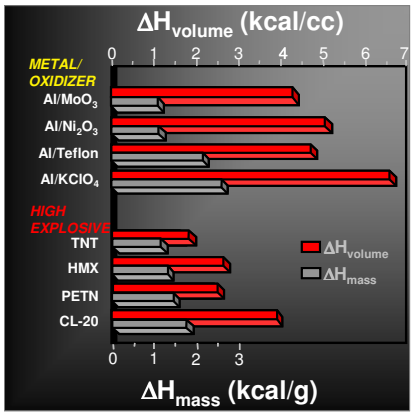

Figure 1-2: Graph describes enthalpy of reactions of Al with various oxidizers in comparison to monomolecular high explosives, per weight and per volume.[8]

Because the energy/enthalpy released is fixed by the reaction equation, researchers are left to determine how to mix the two materials and to assess the most appropriate shapes/sizes/volumes.

1.4 Energetics and the Nano-regime

In the past, thermites contained micron to millimeter scale mixtures of metal and metal oxide particles. Ideally desired is an even distribution of metal and metal oxide throughout the powder. This is true for particles of any size. We shall see that moving into the nano regime can achieve drastic increases in burn rates of thermites. A 5 to 10 fold increase in burning rates has been observed transitioning from micro- to nano-aluminum particles in a propellant mixture[9]. Aumann et al reported a 1000x increase in the reactivity of nano-aluminum compared to micron[10]. The basic motivation for transitioning to smaller sized particles is to decrease the mass diffusion length; the smaller the particles, the closer the fuel and oxidizer. Moreover, with increased surface area to volume ratio and contact area between the fuel and oxidizer, the reaction rate will

rise. This behavior has been detected since mid 1990s and since, there have been a few proposed models that explain what happens in the transfer to nanoscale.

1.4.1 Metal Fuel: Why Aluminum?

In the thermite reaction, aluminum is often the most studied and well characterized fuel. Its practicality originates from its significant energy density as well as the availability of its raw state and methods to synthesize it. Because of this, aluminum is often considered relatively low cost[11]. See Table 1-1.

Metal	**ΔH per unit Mass (Kcal/g)**	**ΔH per unit Volume (Kcal/cc)**
Boron	-14.12	-33.19
Beryllium	-15.88	-29.38
Aluminum	-7.41	-20.01
Titanium	-4.71	-21.20
Vanadium	-3.64	-21.69
Magnesium	-5.91	-10.28
Nickel	-0.98	-8.72

Table 1-1: Comparison of enthalpy of combustion for various metals.[12]

In the energetic world, aluminum is most commonly found in a propellant mixture or as an additive in a monomolecular high explosive. Using aluminum in a propellant will reduce the ignition temperature because of its low melting point, 660ºC. From Table 1-1, it is clear the aluminum is not the only metal fuel to have a large energy density.

Beryllium is quickly ruled out because of its toxicity; while nanoscopic boron shows promise and its reactivity has recently been explored in Sullivan et al [12].

It is clear that a system capable of cheaply generating large quantities of aluminum nanoparticles would be very desirable. Although nano-aluminum is currently commercially available, it is very expensive, on order of thousands of dollars per kilogram. But it is a commercial process that will increase its use as a viable fuel in large scale production.

The drawback of using nanoscale aluminum particles is the self passivation layer of oxide. Aluminum is very easily oxidized, owing to the reason it is most often selected as a fuel, thus when exposed to air under ambient conditions an oxide layer forms on its surface. The thickness of this layer is around 2-5nm independent of particle size[13-16]. In a micron size aluminum particle this oxide shell is relatively small and insignificant, whereas it has a strong influence on nano-aluminum and can represent a majority of the particle's weight. Commercially available 100nm aluminum powder known as ALEX has around 80-90% weight aluminum. This percentage only drops when a smaller size distribution is required. This is one of the biggest challenges for producing an effective nanoparticle containing a substantial percentage of useable material. Unfortunately the passivation of nano-aluminum, while degrading performance, is necessary as it might otherwise spontaneously combust in air[11; 17].

At this time there are no known commercially produced oxide-free aluminum nanoparticles on the market. It is this void that drives the research in passivating the aluminum surface prior to exposure to air. Jouet et al have examined the attachment of perfluorocarboxylic acids to aluminum, with the benefit of combining successful

passivation with an addition energetic compound. The fluorinated acid provides increased energy to the system while preventing Al_2O_3 formation[18; 19].

1.4.2 Metal Fuel: Why Nickel?

Nickel in the energetics world is often not given a lot of attention. Its energy density is outperformed by all the metal fuels in Table 1-1. When formulators first discovered the addition of aluminum to high explosives or propellants increased the time scale of a pressure pulse and flame temperature, the majority of the follow up research was aimed at tailoring the aluminum [20; 21].

Very quickly, researchers realized that the while the addition of aluminum to propellants increased the specific impulse of a rocket motor, the amount of smoke generated was many times greater. Now when a rocket is fired, its trail can be followed back to determine where it was fired from. Obviously this is bad from a military stand point. The increased smoke is actually the condensing aluminum oxide (Al_2O_3) products expelled out the rocket tail[22]. These formulations are still used but the users accept the increased smoke for the increased rocket range.

In a study the addition of nickel nanoparticles (.01% by mass at 100nm) are added to various propellant mixtures (all sans aluminum) to probe the smoke and pressure generated. At lower pressures, analogous to when the rocket is just starting to ignite, the nickel enhanced propellant greatly outperforms, with increased adiabatic flame temperatures and volume of gas evolved. These two characteristics are very useful in initiating a rocket motor. The nickel-propellant also shows increased heat of combustion at lower pressures in comparison to propellants with no nickel. It is observed the addition

of nickel nanoparticles to propellant compounds is extremely beneficial to the initiating/low pressure regime of a rocket motor[22].

We are already aware of the detrimental effect smoke can have on the use of a rocket motor. In propellants without aluminum, smoke is formed physically by the products of reactions and chemically by the nucleation of water around the HCl given off by the propellant burning[6; 7; 20]. Nickel is believed to have the ability to catalyze these physical byproducts and reduce smoke output. This smoke suppression behavior is observed in nitrocellulose-nitroglycerin double base (NC-NG) propellant igniters containing nickel nanoparticles in comparison to a boron-potassium nitrate mixture. Also the increased heat of combustion observed before, means where a double base NC-NG alone fails to ignite a rocket motor, the nano-nickel compound can successfully burn. While nickel has interesting smoke reducing properties, the pressures and burning rates generated through its addition are easily outperformed by aluminum[22]. Currently the trend in explosive research is toward the latter.

Chapter 2: Literature Review, Precursor Selection, and Experimental System

Our research goal was to produce both oxide passivated and pristine aluminum nanoparticles that would be later coated. There are actually multiple ways of producing aluminum nanoparticles; this research focuses on the thermal decomposition of a chemical precursor as the source of aluminum. When ideal aluminum nanoparticles could not be generated, an investigation into iron oxide coated nickel nanoparticles was undertaken. Nano-nickel exhibits interesting optical[23], magnetic[24], chemical[25] and energetic[22] properties. We already know from Table 1-1, that nickel can be used as an energetic, but it lacks the energy density of aluminum and other metals.

2.1 Gas Phase Methods for Generating Metal Nanoparticles: Aluminum and Nickel

Aluminum and nickel have been previous generated in situ by varying methods, both gas and liquid based. This literature review will focus on the synthesis of aluminum and nickel nanoparticles/nanostructures in the gas phase. One of the simplest methods relies on the evaporation of metallic aluminum in an inert gas flow. Fresh aluminum is heated to obtain a desired vapor pressure of aluminum gas. Inert gas is passed over the material and carried downstream, where it is cooled and aluminum nanoparticles are formed[26; 27]. The same evaporation method can be applied to nickel.

While the particle size can be sub-10nm, the quantity of particles produced compared to the amount of energy used to evaporate aluminum or nickel is very poor; thermal resistive

heating and laser ablation have hefty power requirements that don't usually scale well. However quasi-evaporation techniques have been improved to produce large quantities. This commercial method involves the arc discharge across an aluminum target or wire to evaporate the aluminum gas. A simple but effective way to generate metal nanoparticles is called DC Arc or Electric Explosion of Wire (EEW) method. A diagram of this the DC Arc setup is shown here:

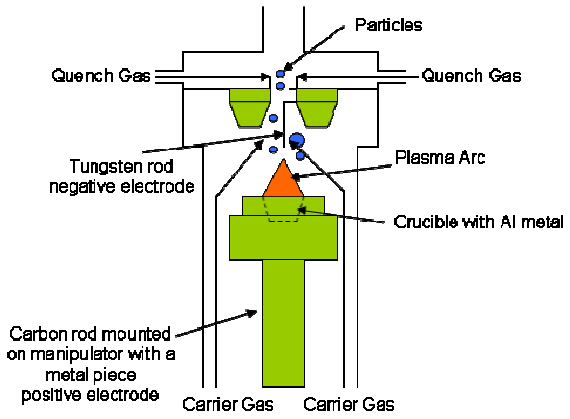

Figure 2-1: Diagram of DC Arc method, shown with aluminum. [28]

The basic principle of the synthesis is that a large potential is generated across two electrodes (or one electrode and a wire of desired metal for EEW), which in-between lays the desired metal. In Figure 2-1 aluminum is labeled in the crucible. A plasma arc forms between the two electrodes and inert carrier gas. This arc causes the ejection of aluminum atoms or small agglomerations of such from the bulk material. They are then carried to an inert cooling quench gas that promotes nucleation and growth. The size distribution of these particles is controllable by current but weakly[28].

Recently Liu et al performed studies on the laser ablation of a pure nickel target to create crystalline nickel nanoparticles. They observed two types of particles, a spherical nickel core and nickel oxide shell, and cubic nickel oxide[29]. The high temperature

plasma created at the bulk nickel surface commonly leads to partially oxidized particles because the source gas can never really be oxygen free.

Research focus transitioned away from adapting bulk materials to finding suitable chemical precursors which could be decomposed to metallic aluminum/nickel. Precursor selection will be discussed later. When generating gas phase metals from a chemical precursor, a lot of the basics are independent of design. A precursor molecule must contain atom(s) of the desired metal and are typically metal organics (e.g. triethylaluminum, metal carbonyls…) or metal halides (e.g. aluminum trichloride…). The geometry of the setup differs from lab to lab, but in general the solid or liquid precursor is heated to obtain a larger vapor pressure. An inert carrier gas is then passed through or over this material and the vapor phase of the precursor is carried out[3; 30].

Alternatively if the precursor is liquid or can be combined with solvent, the solution can be directly aerosolized. Several methods exist to accomplish this; nebulizers, spray atomizers, and flame generators all physically eject droplets or particles[31].

Liquid pressurized atomizers have various designs but all feed a pressurized liquid, and if needed compressed gas, through a nozzle to a lower pressure environment[32]. The droplet distribution formed is reliant on the liquid's physical proprieties, flow rate of liquid/gas, and nozzle design[31]. Often the droplets produced are much larger than the desired final distribution. Passing the aerosol through appropriate diffusion dryers can draw the solvent out of the droplets causing it to shrink[33-35]. An advantage of a sprayer system is that large quantities of materials can be produced relatively simply.

Other methods to produce aerosols do not require high pressures or specially designed nozzles. Specifically, piezoelectric nebulizers generate ultrasonics in a

precursor causing droplets to be ejected from the liquid's surface. The nebulizers are commonly available as personal humidifiers and can be modified to generate droplets of a supplied precursor solution[31]. Because the hardware is widely available, this method is established with little trouble.

Once an aerosol is obtained the vapor and inert gas are usually exposed to a heating source to provide thermal energy. In this examination we strictly used tube furnaces to rapidly decompose the precursor, exposing the metal atom(s). In other systems, a plasma is used to completely dissociated the precursor into its elements[30]. Ultraviolet or visible lasers have been used in the photolysis of a precursor. If the carrier gas is invisible to the wavelength of light, only the precursor molecule is heated[36-38]. Once decomposed, the metal atoms then nucleate to a critical size where surface growth takes over. Size distribution is often controlled by the concentration of precursor/metal atoms in vapor phase, the time and rate at which they condense/cool, and chemistry of precursor and carrier gas[2; 3].

2.2 Selection of Aluminum Precursors

Much of the precursor selection has been narrowed by the semiconductor industry, where the controlled chemical vapor deposition of aluminum is desired. Because of its low cost and variety of deposition techniques, aluminum is a popular material for interconnects in microelectronics. Most aluminum precursors fall under two categories aluminum alkyl and alane (AlH_3) complexes [39; 40]. They are very volatile when reacting with water and oxygen. Some including TEA are pyrophoric and spontaneously combust in air[39]. Traditionally metal halides, such as aluminum trichloride, were not

generally regarded as suitable precursor materials for the metallic counterparts as a lack of literature shows [39-41].

The trivalent nature of aluminum means a precursor will contain three anionic ligands. A ligand's size and resultant steric effect determines the monomeric, dimeric or trimeric structure of the precursor. Trimethylaluminum (TMA) with relatively small methyl group will favorably form a dimer structure, while an isobutyl ligand in trisobutylaluminun(TIBAL or TIBA) will remain monomeric[39; 42].

2.2.1 Alane Precursors

Alane precursors lack the Al-C bond and decrease greatly the likelihood of carbon impurities. Aluminum is only bonded to nitrogen and hydrogen, weaker bonding than to carbon[38; 39]. Because the bond energy is lower for Al-N, it can be cleaved simply without an extraneous low energy dissociation mechanism[39; 43]. Dimethylethylamine alane (DMEAA) and trimethylamine alane (TMAA) have emerged as popular alane complexes for Al CVD[38; 41]. The steric hindrance of DMEAA and TMAA imposes a monomeric structure. Often these alane compounds have higher vapor pressures than aluminum alkyls, but less long term thermal stability even at ambient temperature[44].

The simplified and lower energy decomposition pathway for alanes, means substrate temperatures as low as 100ºC have been used with DMEAA and TMAA[43]. Conversely, TIBAL, an aluminum alkyl cleaves in substrate temperatures 200 ºC to 400ºC[39; 45].

2.2.2 Alkyl Precursors

Aluminum alkyls contain usually three Al-C bonds. In their decomposition, the Al-C bond is strong enough to prevent its straightforward thermal cleaving and lower

energy mechanisms are required for the production of metallic aluminum. This mechanism is often beta-hydride elimination[39].

The decomposition of TIBAL proceeds once the molecule has absorbed on an aluminum surface, where the transfer of isobutyl ligands to other aluminum atoms proceeds beta hydride elimination; free H_2 and isobutene are given up in this reaction[39; 45]. At higher temperatures, above 330 ºC, beta-methyl elimination might take place, leaving methyl group to decompose into methane, hydrogen and carbon contaminated aluminum[45].

Trimethylaluminum (TMA) is observed to be a poor precursor for aluminum CVD, lacking a lower energy Al-C decomposition pathway. The methyl group is unable to undergo beta-hydride elimination[39; 45]. To cleave this molecule a high temperature process is required, promoting the concentration of free carbon.

Dimethylaluminunm hydride (DMAH) is an extensively used precursor for aluminum CVD process. At room temperature, its relatively high vapor pressure and low viscosity make it ideal for high rate gas production of aluminum using a bubbler system. In practice the bubbler/precursor source is heated to obtain a larger vapor pressure, in which DMAH response nicely. However its viscosity even at 50ºC is no longer stable, thickening up even after a few days[46].

The decomposition of DMAH was believed to take place through hydrogen reduction, requiring a carrier or addition flow of hydrogen gas[47; 48].

$$2DMAH + H_2 \rightarrow 2Al + 2CH_4 \qquad (2)$$

Amazawa showed successful Al film growth using DMAH without hydrogen gas, proposing DMAH directly thermally decomposed[46].

$3DMAH \rightarrow 2Al + TMA + 3CH_4$ (3)

The instability of the DMAH viscosity over an appropriate amount of time, and questioned decomposition pathway are why it was avoided in this investigation.

Triethylaluminum exists in both monomeric and dimeric structure in the liquid and gas phase[42]. Unlike a methyl ligand, an ethyl ligand can undergo beta-hydride elimination, increasing the promise of TEA as a low temperature aluminum precursor. The purposed beta-hydride elimination of TEA is shown in Figure 2-2.

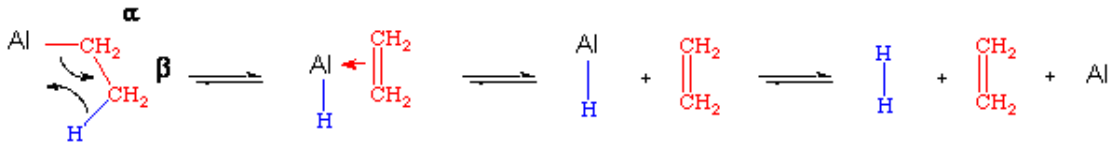

Figure 2-2: Beta-hydride elimination of an ethyl ligand on Al. (self made)

2.3 Selection of Nickel and Iron Precursors

2.3.1 Nickel

Nickel has received less research attention than aluminum in CVD and other similar processes. One common precursor that has been used to create gas phase nickel nanoparticles is nickel carbonyl. The decomposition of nickel carbonyl has been shown since the 1960s by Boldt [49]. Nickel carbonyl is useful in gas phase procedure because it boils at a reasonable temperature, 50 ºC. In He et al a flow nickel carbonyl is exposed to a UV laser, rapidly decomposing it to nickel and carbon monoxide[37]. Because the source gas and carbon monoxide does not absorb the UV light, the reaction essentially takes place at room temperature. The thermal decomposition, kinetics and pathways, of nickel carbonyl have also been well studied[50; 51].

Nickelocene, $Ni(C_5H_5)_2$, a metalorganic used in the MOCVD of nickel films is alternative to nickel carbonyl. In inert environment, $NiCp_2$ is volatile, but thermodynamically stable[52]. It has been looked at for large scale processing, because it is not cost-prohibitive or as toxic as carbonyls[53].

In the gas, Brissonneau et al have reported lack of understanding of its decomposition through hydrogen reduction. For thin films of nickel, substrate temperatures of 150ºC to 350ºC are probed for the desorption of C_5H_n, a sign of successful decomposition[54]. Actually decomposition occurs at the melting point of 173ºC, with the reaction

$$Ni(C_5H_5)_2 + nH_2 \rightarrow Ni(s) + 2C_5H_{5+n}(g) \text{ for } n= 0,1,3,5. \quad (4)$$

Without the addition of hydrogen, $NiCp_2$ will not decompose below 200ºC [55], while nickel carbonyl requires no hydrogen to produce metallic nickel.

A more recent approach to generating an aerosol nickel nanoparticles employs the spray pyrolysis of a hydrated nickel nitrate solution with various co-solvents. It is the reducing agents, ethanol, formic acid and H_2, that makes it possible to synthesize mostly oxide free nickel nanoparticles; evidence is provided by weak NiO and strong Ni XRD peaks [56]. A spray pyrolysis system first aerosolizes the precursor solution, if desired the droplets and carrier gas pass through dryers to remove water. If highly oxidized particles are preferred, the water is left in. The aerosol is heated, reducing nickel nitrate to nickel. Because of the increase surface area of nickel nanoparticles and remaining water in the process, NiO is presents in a composition analysis.

2.3.2 Iron

Iron pentacarbonyl is a metalorganic used fairly extensively as a precursor for iron nanoparticles because it can be easily decomposed at relatively low temperatures with no unwanted byproducts. Although the breakdown of iron pentacarbonyl is easy, the reaction pathways and rates are complicated and not strictly studied. These rates and reaction order are dependent on the particulars of the process and vary [57].

Working in the gas phase simplifies the process even more. By eliminating solvents, the only solids produced are the iron particles while carbon monoxide and carrier gases can be readily exhausted[58; 59]. Karlsson et al investigated evaporated iron pentacarbonyl decomposed at 740ºC, 1070ºC, and 1280ºC, while surveying the relative sintering of the iron nanoparticles over the temperatures 25ºC, 740ºC, 850ºC, 960ºC, and 1200ºC[60]. They note "conductive deposits" building up in their instruments at 250ºC, a good indication that decomposition reaction was not complete.

This gas phase particle formation can be compared to a solvent based approach where iron pentacarbonyl is decomposed in kerosene over 160ºC-180ºC. Shao et al noticed with an increasing solvent temperature a decrease in particle size was observed[61]. Comparing Shao and Karlsson's work it is likely that iron pentacarbonyl's reaction pathway, and the rate and energy needed for decomposition might vary greatly from liquid to gas phase. Owing to our gas phase experiment we will pay more attention to Karlsson's decomposition temperature.

Other iron metalorganics, that can be thermally decomposed at reasonable temperatures, have been used to synthesize iron nanoparticles. On such precursor, $Fe[N(SiMe_3)_2]_2$, which is decomposed at 150ºC in hexadecylamine and, oleic acid or

hexadecylamonium chloride over 48 hours[62]. While the time span of this reaction can not be reasonably applied to a gas phase reaction, the product is a nearly monodisperse yield of 7nm or 8nm nanocubes; a unique consequence of this technique.

2.4 Precursors and Experimental Setup

The two aluminum precursors we will investigate are triethylaluminum (referred to as TEA or $Al(Me)_3$) and aluminum trichloride ($AlCl_3$). The vapor phase of liquid TEA will be extracted from a bubbler, while the solid $AlCl_3$ will be used in a packed bed of two different designs. We believe generation of Al nanoparticles by thermal decomposition, in a tube furnace, of these materials has not been explicitly shown in literature. Bin Zhang's 2007 dissertation [30] comes close but $AlCl_3$ is decomposed in a plasma synthesis technique. I point this particular study out because of how close it is related to my research and we believe we have identified a potential error/fault in the preparation of their system.

Core-shell nickel/iron oxide nanoparticles will be synthesized from nickel carbonyl and iron carbonyl. Nickel carbonyl is sourced in-situ from a nickel/carbon monoxide packed bed, while iron pentacarbonyl is evaporated or bubbled with argon.

The equipment used the experiment include the following:

- MKS Power Supply and Readout
- MKS Flow Control units (calibrated to our system)
- Epichem 500g bubbler
- Lindberg/Blue Tube furnace(s)
- Omega Silicon Rubber heating tapes

- Variable AC voltage transformers
- Household insulation
- Inline K-type Thermocouple(s) and Reader
- Inline Omega Pressure Transducer
- Home Built Packed Bed(s)
- TSI Long DMA
- TSI CPC
- Millipore and Nucleopore filters and housings
- Various Swagelok hardware

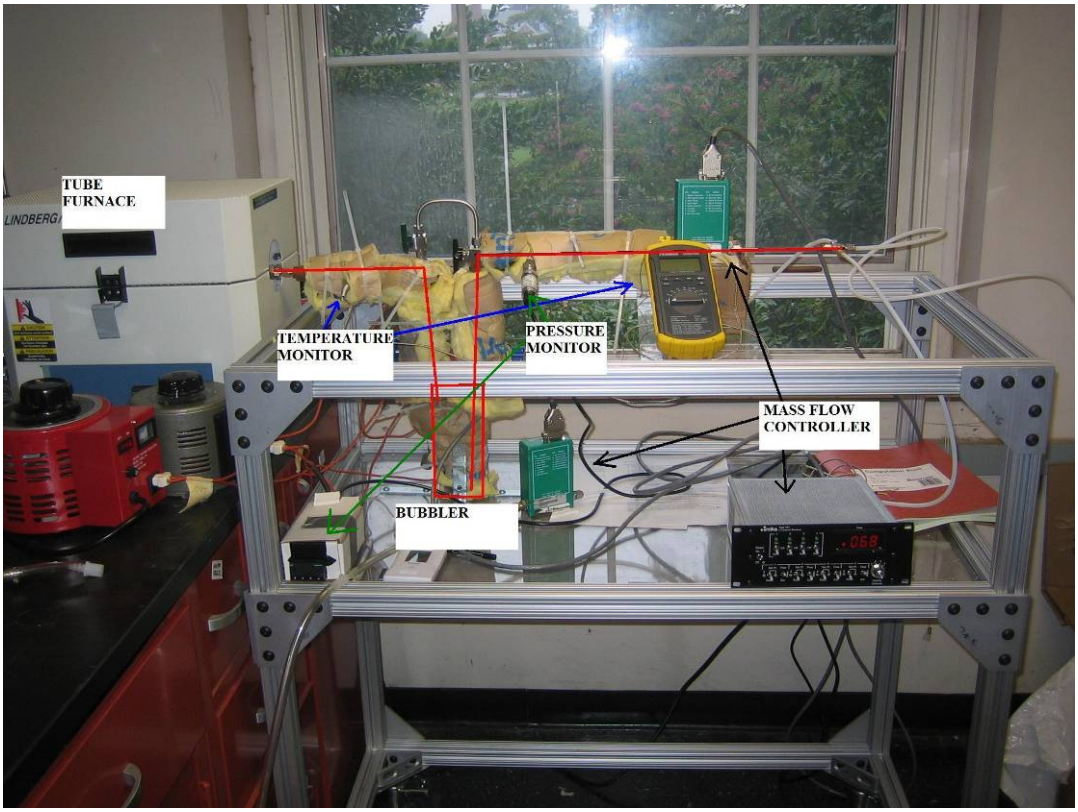

Figure 2-3: Diagram/photo of the bubbler setup. Note with $AlCl_3$ the bubbler is replaced by a packed bed not shown.

Chapter 3 Triethylaluminum Investigation

The triethylaluminum (TEA) was sourced from and filled by Jason Jouet at the NSWC, Indian Head and originally from Sigma Aldrich. TEA is highly pyrophoric and must be handled with extreme caution while avoiding contact with air. It has been previously reported to decompose at 162-192ºC [63].A system was assembled around the bubbler described in Figure 3-1.

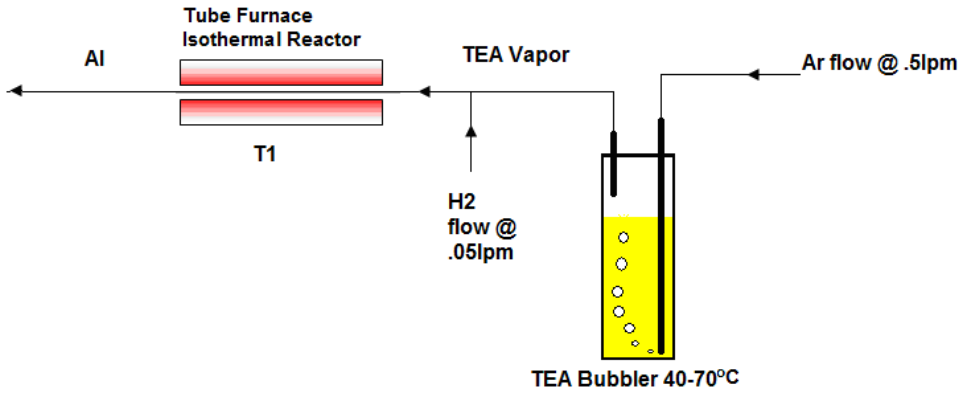

Figure 3-1: Diagram of TEA bubbler system.

The stainless steel lines carrying the vapor from bubbler to tube furnace are heated to temperature above that of the bubbler/vapor. Over the course of the experiments, the temperature of the bubbler was varied from 40º to 70 ºC. Temperature of the lines and bubbler are monitored by thermocouples, meaning we track the temperature of the gas being carried out and liquid TEA inside the bubbler. It is safe to assume the vapor TEA initially exiting the bubbler is at the same temperature of the liquid TEA, and thus have same vapor pressure. Combined with the argon flow rate, we are able to control the amount of TEA introduced to the reactor. Theoretical production rates are calculated from ideal gas law using flow rate and vapor pressure of TEA via temperature of bubbler.

These rates represent the maximum amount of material able to be produced and ignore losses to tube walls, but are helpful to determine the industrial/production viability of a precursor.

0.5 Lpm		**TEA**	**Al**
Vapor Pressure	**Temp**	**g/hour**	**g/hour**
Pa	**ºC**		
15.2	40	0.02	0.005
37.7	50	0.05	0.011
88.1	60	0.11	0.026
413.3	80	0.48	0.114
1 Lpm		**TEA**	**Al**
Vapor Pressure	**Temp**	**g/hour**	**g/hour**
Pa	**ºC**		
15.2	40	0.04	0.01
37.7	50	0.01	0.023
88.1	60	0.22	0.052
413.3	80	0.99	0.228

Table 3-1: Theoretical production rates of aluminum from TEA bubbler.

3.1 Clogging of TEA

A characteristic of both systems is that all of the lines carrying the precursor vapor need to be heated to at least above the temperature of the packed bed/bubbler to prevent condensation. Condensation of precursor material before decomposition will have negative effects on production efficiency and system reliability.

On particular problem of reliability of the TEA/bubbler systems was the clogging of valves. After ~50 hours of operation, pressure inside the bubbler and input line would build to the pressure at the argon tank; this was remedied by dissembling and physically cleaning the valves inside an inert glove box. Inspecting the valve assembly revealed that clogging was the result of condensation and degradation of TEA at this point. This could be attributed to either the use of a lower purity argon or heating of the valve reached too high of a temperature and caused internal decomposition of the TEA. We did not investigate this further as TEA precursor failed to produce containment free aluminum particles.

3.2 Product Analysis

Transmission electron microscopy (FE-TEM, JEOL 2100F) was conducted on a sample run at a bubbler temperature of 62.5 ºC, furnace temperature of 450 ºC and flow rate of .5 LPM. The sample mass was first collected on Nucleopore filters (47mm, .2 micron) on a Millipore filter housing over 60 minutes in which a small amount of air is bleed into. A black powder was observed and confirmed to burn, indicating presence of an energetic material. A small amount of material is mixed with 10ml of hexane and sonicated for 10-15 minutes to disperse the particles in solvent. A drop of solution is then deposited on a Formvar coated copper TEM grid.

3.2.1 Decomposition at 450ºC

The images below show intriguingly, two particles sizes and structures. Smaller particles (25nm-75nm), believed to be aluminum, appear to be ‘sticking’ to the larger

porous looking particles (125nm-150nm). This behavior remains still unexplained. It is noted that the aluminum particles appear both as spherical and cubic-like structure.

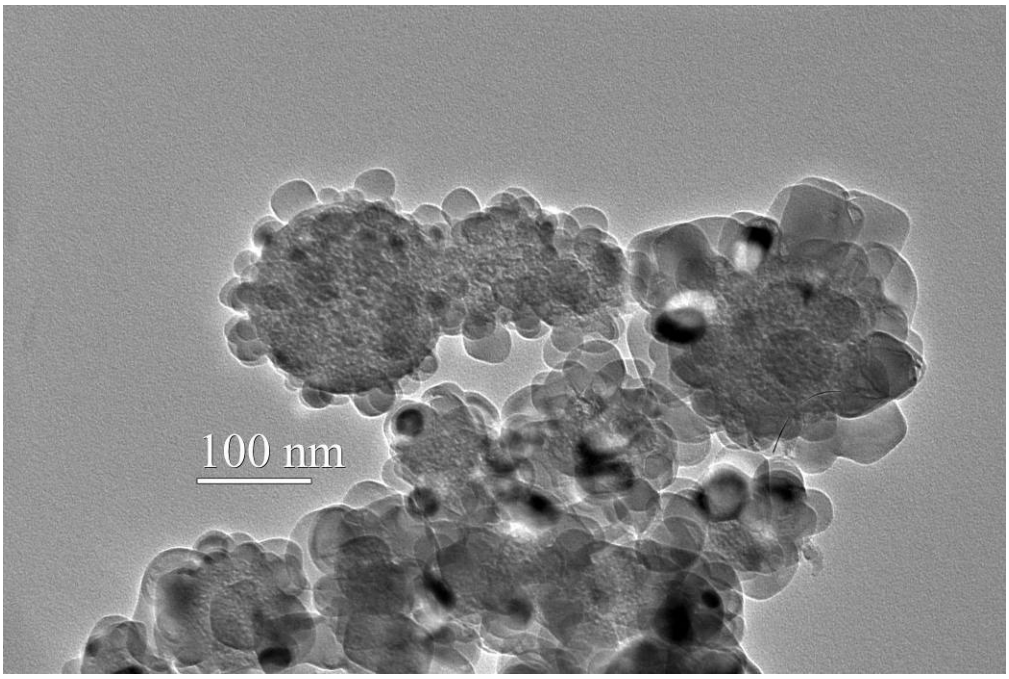

Figure 3-2: TEM image of aluminum nanoparticles and containment at 450ºC furnace.

3.2.2 Decomposition at 750ºC

A second sample was collected at bubbler temperature of 65.4ºC, furnace temperature of 750ºC and flow rate of .5LPM. The same two particle structures are observed, except the cubic-like particles have been the suppressed and the larger particles of unknown composition have slightly increased in size (150nm-225nm).

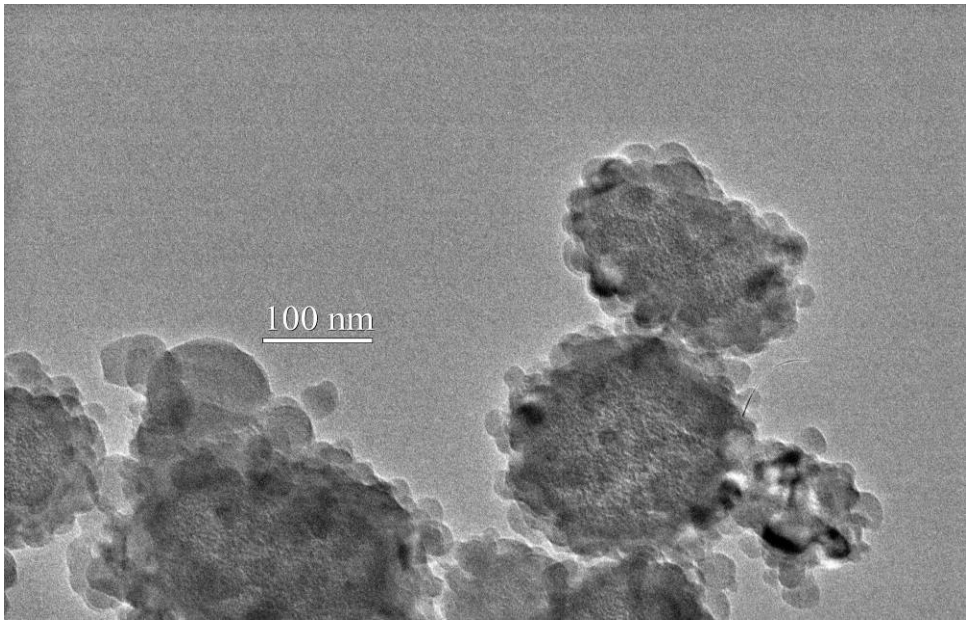

Figure 3-3: TEM image of aluminum nanoparticles and containment at 750ºC furnace.

Further examination of the sample cracked at 450ºC reveals the passivation of the aluminum particles by an oxide layer, approximately 5nm thick. The conditions for this passivation were that collected sample was simply exposed to air at ambient or slightly elevated temperatures. Figure 3-4 illustrates this core-shell behavior.

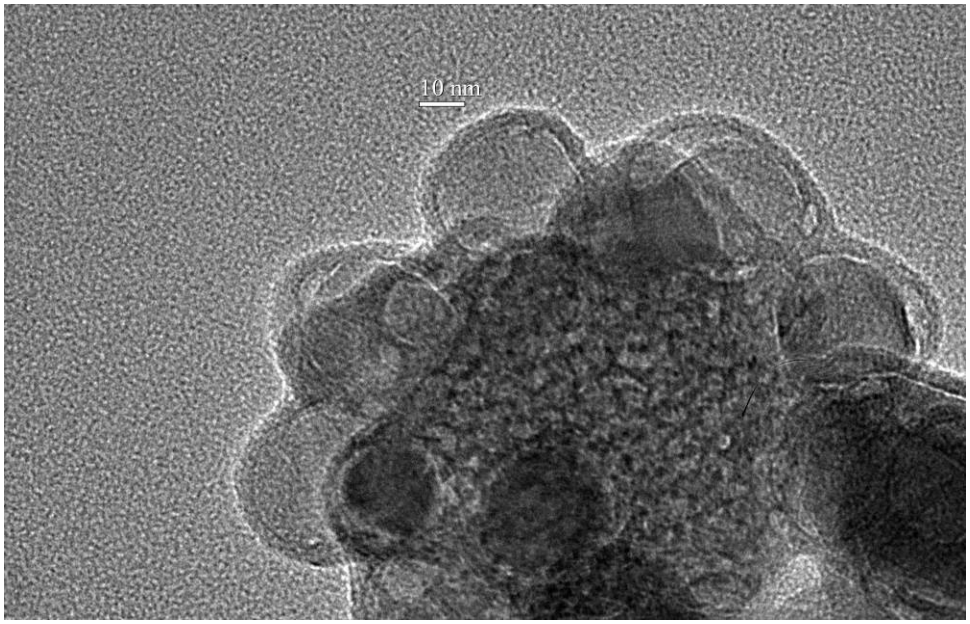

Figure 3-4: High Magnification of 450ºC sample showing oxide shell on aluminum nanoparticles.

3.3 Energy Dispersive X-ray Spectroscopy

Compositional analysis was performed by energy dispersive x-ray spectroscopy (EDS) concurrent with TEM. In Figure 3-5, a 2D EDS feature is used to map the composition of the particle. The smaller particles were confirmed to be aluminum. Oxygen was also observed on the particle, consistent with an aluminum oxide layer and is likely to be Al_2O_3. The presence of carbon is relatively constant throughout scan (excluded from Figure 3-5) indicating that the Formvar grid is responsible. Formvar, or polyvinyl formal, contains both carbon and oxygen so strict examination of these elements is further complicated.

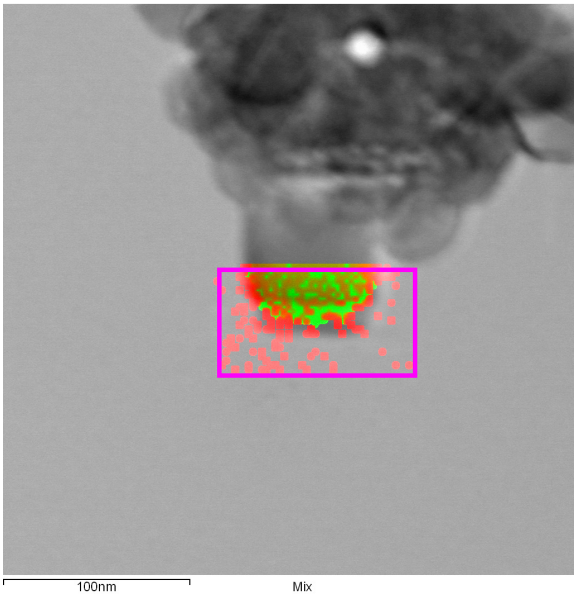

Figure 3-5: TEM/EDS analysis of aluminum nanoparticle; Green--Aluminum, Red--Oxygen.

The exact composition of the center (larger) particle remains unknown. A direct and exact EDS measurement of the particle is prohibited because the surface of said particle is covered by the smaller aluminum particles. As seen in Figure 3-6, the level of drops off as the e- beam (5nm spot size) leaves the unknown particle, while carbon remains relatively constant and aluminum fluctuates; possibly due the smaller aluminum particles stuck the surface.

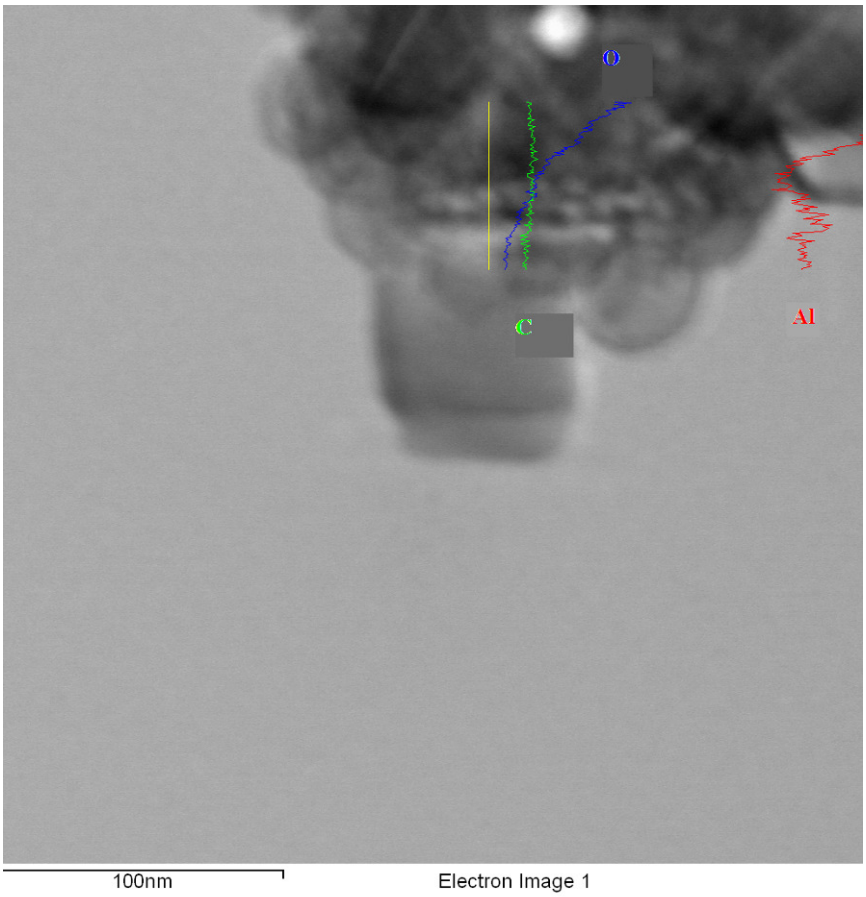

Figure 3-6: EDS of unknown carbon contaminant with surface aluminum particles.

But we can still say it contains carbon, oxygen, and possibly aluminum, while no other elements are found. It is possible that the newly freed ethyl groups, in presence of hydrogen, polymerize to form this porous looking structure. This has not been confirmed. Under the TEM this structure is highly reminiscent of carbon soot. A similar precursor trimethylaluminum, when decomposed can contain unwanted aluminum carbide, Al_4C_3[40; 46]. Although the structure of the unknown particle does not demonstrate any crystallinity, Al_4C_3 can not be completely ruled out.

3.4 Decomposition below 450ºC

When the furnace is run at temperatures below 450ºC a white powder is collected when air is bleed into the filter. This powder is non reactive and does not burn, unlike the black powders collected above. TEM images of this white powder reveal a porous structure, which is most likely uncracked TEA reacting with ambient air. When collecting significant quantities of material without bleeding air into the filter, the filter paper is covered in a dark yellow liquid which upon exposure to air quickly burns and melts.

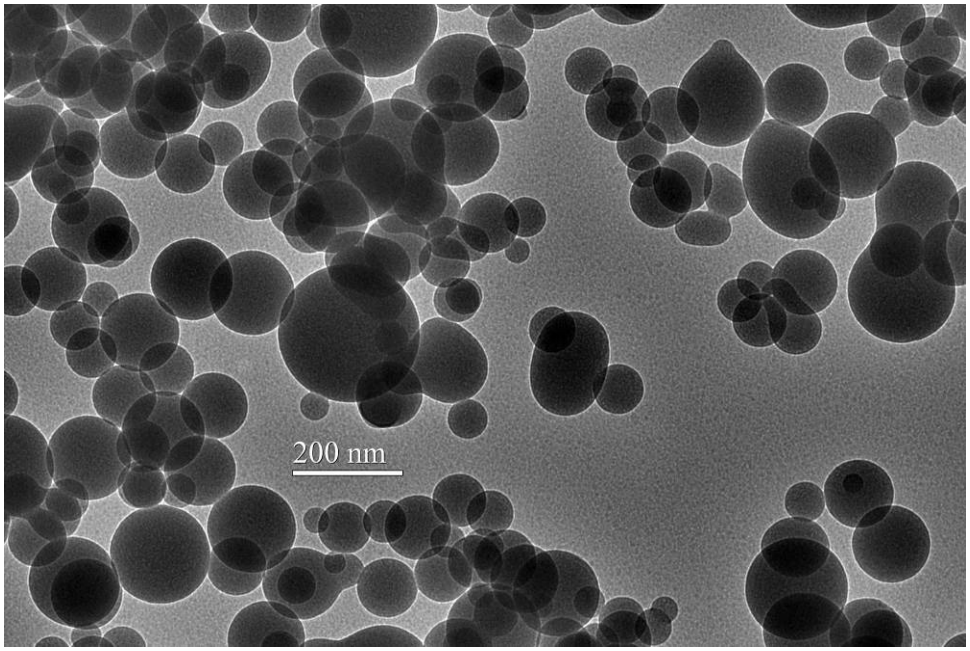

(a)

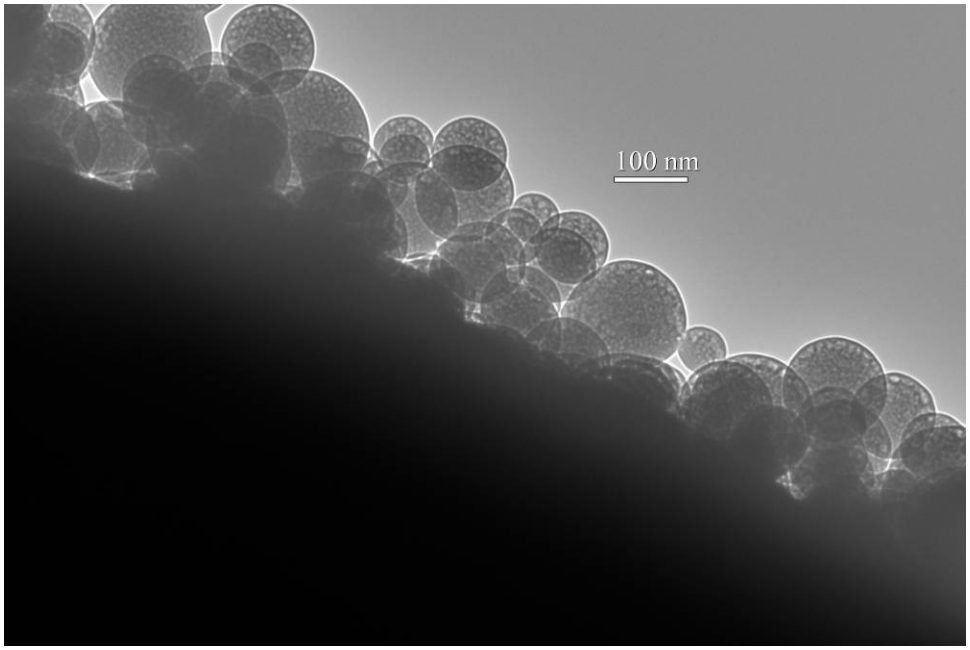

(b)

Figure 3-7: (a) and (b) TEM of TEA particles run at furnace temperature of 300ºC

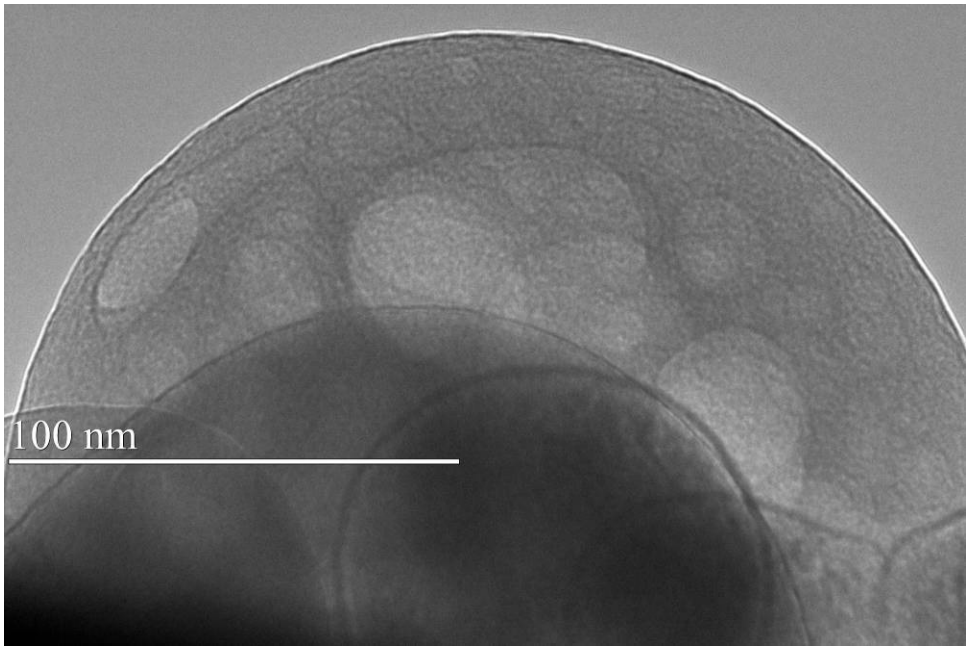

Figure 3-8: TEM of TEA particles run at furnace temperature of 300ºC, with pitted surface and porous structure

In our investigation into the thermal decomposition of triethylaluminum, we have been able to show the generation of aluminum nanoparticles inherently mixed with a larger carbon, oxygen and possible aluminum contaminant. At this point, we are unable to suppress or eliminate the presence of these particles. Originally, we believed that the decomposition of TEA with hydrogen would proceed as:

$$AlC_6H_{15} + 9/2H_2 \rightarrow Al + 6CH_{4\ (g)}$$

This was probably an oversimplification of the reactions. Most likely the temperatures needed to cleave the aluminum-carbon bond, also break the carbon-hydrogen bond; the presence of carbon or polymerized ethyl groups is then expected. All attempts to lower the furnace temperature to eliminate the contaminant do not decompose the TEA.

Chapter 4 Aluminum Trichloride

4.1 Packed Bed and $AlCl_3$ Decomposition Background

In addition to exploring triethylaluminum as a chemical precursor for aluminum, we investigated aluminum chloride (referred to as aluminum trichloride or $AlCl_3$). $AlCl_3$ (Sigma-Aldrich, purum anhydrous, ≥98.0%) is currently around ten times cheaper than TEA, making it increasingly economical for a large scale process. Ultimately, two different systems to house the $AlCl_3$ powder were attempted. System one, seen in Figure 4-1, employs a horizontal packed bed, mixing $AlCl_3$ and borosilicate beads (Sigma-Aldrich, 3mm dia.) confined with fine steel mesh on ether side. Borosilicate beads serve to break up the powder and prevent the carrier gas from creating uninterrupted paths through the material. These 'cracks' or paths reduce the quality of the assumption that vapor phase inside the bed is equal to the vapor pressure being carried out.

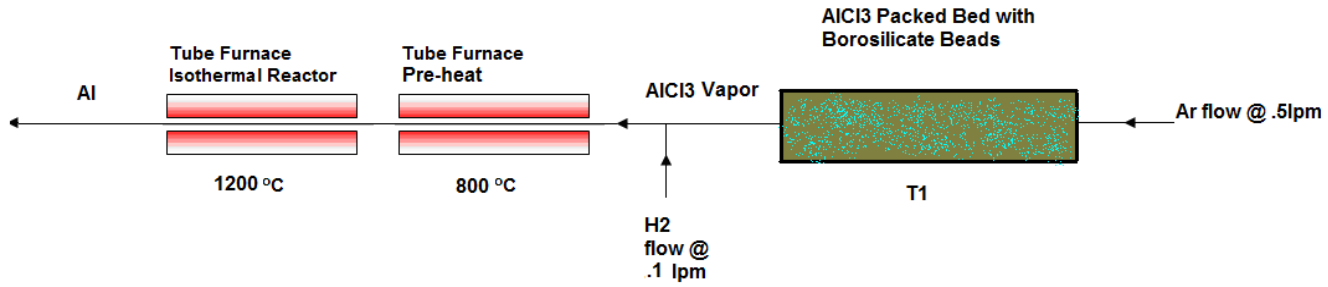

Figure 4-1: Diagram of $AlCl_3$ packed bed system (not to scale).

No literature was found examining the non-plasma decomposition of $AlCl_3$ in absent of oxygen or nitrogen. Demonstrating the formation of pristine metallic aluminum from $AlCl_3$ would be nascent.

There is a plethora of papers outlining the production of either aluminum nitride ($AlCl_3$ with N_2 and NH_3)[64] or aluminum oxide ($AlCl_3$ with O_2)[65], which provided additional credence to the selection of $AlCl_3$ as a precursor. In these papers, the reactions are carried out at 1200ºC in both gas phase and on substrates. We apply this temperature to our system, citing the previous investigations [64; 66]. Coincidently, our original tube furnace was also limited to 1200ºC. In practice a pre-heat furnace is set at 800 ºC to ensure the aerosol can reach 1200 ºC in the decomposition furnace.

Catoire and Swihart provide a basic and theoretical account of the decomposition of $AlCl_3$ in presence of H_2 and CO_2. Hydrogen is required for the successful decomposition, as it reacts with Cl^- to from non-dissociated HCl [67]. We supply excess H_2 gas post packed bed with flow rates ranging from 0.1 -0.54 Lpm. Formula 5 describes our reaction.

$$AlCl_3 + 3/2H_2 \rightarrow Al + 3HCl_{(g)} \quad (5)$$

Equilibrium vapor pressure is obtained from Stull [68], and is used to calculate theoretical production rates using same methods outlined for TEA.

Calculated ideal production rates			**Production**
	flow rate =.02lpm		
Vp (Pa)	**AlCl3 (grams/min)**	**ºC**	**Al Grams/hour**
1733	0.0015	105	0.0179
2266	0.0019	106	0.0234
2666	0.0022	107	0.0275
2933	0.0025	110	0.0302
3333	0.0028	112	0.0344
6650	0.0056	125	0.0686
29925	0.0253	150	0.3085
	flow rate = .2lpm		
Vp(Pa)	**$AlCl_3$ (grams/min)**	**ºC**	**Al Grams/hour**
1733	0.015	105	0.179

2266	0.019	106	0.234
2666	0.022	107	0.275
2933	0.025	110	0.302
3333	0.028	112	0.344
6650	0.056	125	0.686
29925	0.253	150	3.085
	flow rate =.5lpm		
Vp (Pa)	**AlCl3 (grams/min)**	**ºC**	**Al Grams/hour**
1733	0.0367	105	0.447
2266	0.0480	106	0.584
2666	0.0560	107	0.687
2933	0.0620	110	0.756
3333	0.0705	112	0.859
6650	0.1407	125	1.714
29925	0.6332	150	7.713

Table 4-1: Theoretical aluminum production rates of $AlCl_3$.

In comparison to TEA, this aluminum halide can provide dramatic increases in production rate of our material because of its larger vapor pressure.

4.2 Packed Bed Design #1 with Borosilicate Beads

Our first trials with $AlCl_3$ in the packed bed yielded a strong silicon contaminate. Instead of aluminum particles we were making alumina silicate. The samples were collected on Nucleopore filters (47mm, .2 micron) after 20-30 minutes. Two methods were used to coat the TEM grids: attaching the grid directly to the filter paper exposed to the flow or post-collection, drying a drop of sample sonicated in hexane on to it.

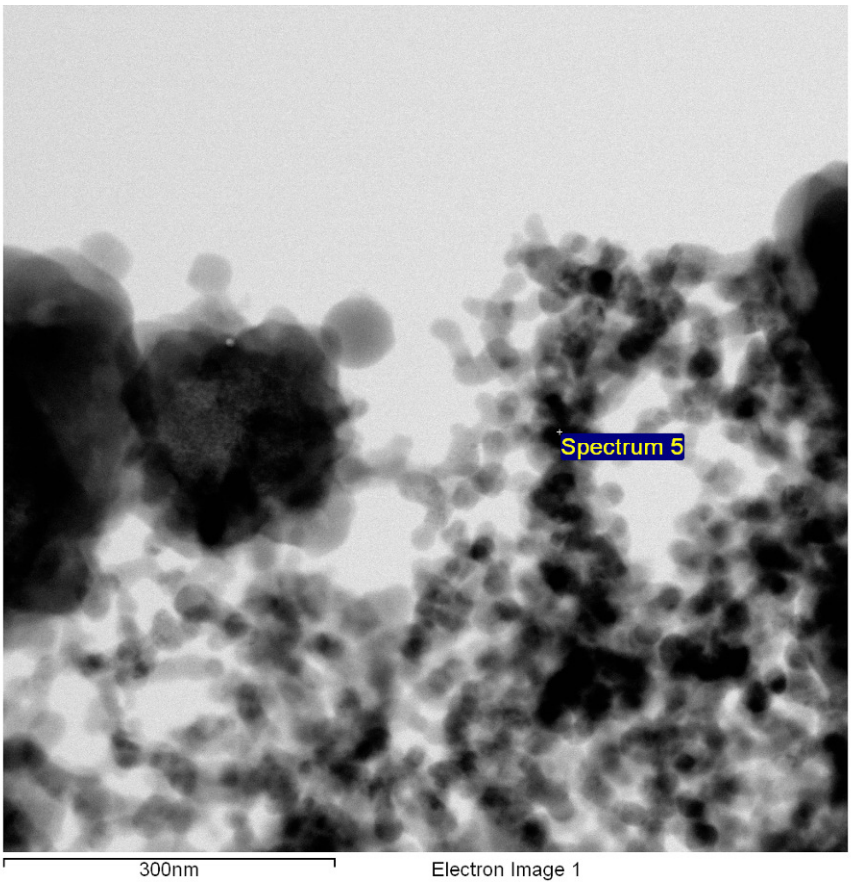

Element	Weight%	Atomic%
C K	49.27	62.00
O K	27.32	25.81
Al K	18.44	10.33
Si K	1.91	1.03
Cl K	0.31	0.13
Ni K	2.75	0.71
Totals	100.00	

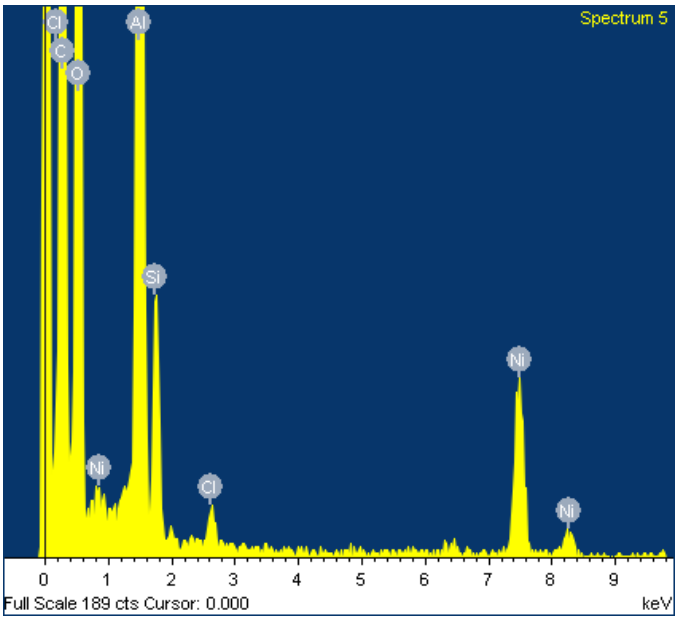

Figure 4-2: EDS of particles from first trial of $AlCl_3$ on carbon coated nickel grids.

At such a high temperature we expect to be sintering our aluminum to larger sizes. The smaller particles above (Figure 4-2) dominate the sample and are believed to be too small to be purely aluminum. EDS analysis showed significant amounts of oxygen and silicon.

Aluminum silicate, a ceramic, has a much high sintering temperature than aluminum metal, which explains the smaller nature of our particles.

4.2.1 Addressing the Silicon Contaminant

A possible source for our silicate contaminant was originally thought to be the alumina furnace tube. At high temperatures, combined with HCl gas, it is likely that the binding material, silicon oxide, can leach out of the tube and into our flow. To correct this, a pure graphite tube liner was constructed to house the flow. But the same particle morphology and silicon contaminate was observed. Eventually we concluded that the source for the silicon was not our furnace tubes, rather the borosilicate beads in the packed bed. Upon inspecting the contents of the bed, the once yellow powder had now turned yellow with spotted orange. The orange substance was located near the beads, lending credence to the idea that the $AlCl_3$ was reacting, albeit slowly, with the borosilicate beads and allowing a silicon oxide contaminate to enter our flow. We note that in the Zhang [30] investigation, a similar setup of packing beads mixed with $AlCl_3$ is studied. They reported, through EDS, the successful generation of aluminum nanoparticles. We point out that the grid used to support the particles was carbon coated silicon nitride (Si_3Ni_4), making the determination of silicon much more difficult.

To remedy our situation, a bead-free packed bed was designed and followed the concept of a bubbler, except our precursor is a solid (hence no bubbles).

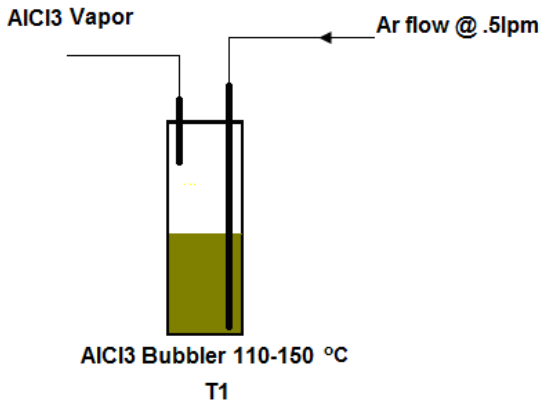

Figure 4-3: Bead-free quasi-bubbler for $AlCl_3$

4.3 Decomposition up to 1600ºC and EDS analysis

Ultimately with this design we are able to show silicon free particles, but not metallic aluminum. A new tube furnace was sourced, increasing the ceiling temperature of our experiment to 1600 ºC. All runs up to 1600ºC fail to successfully decompose $AlCl_3$ to form pure metallic aluminum atoms/clusters. Only a white powder is thermopheretically collected on a quartz tube, post reactor. When this powder is exposed to air, a chlorine scent is detected. This is a strong indictor of hot $AlCl_3$ oxidizing in air, not the generation of pristine aluminum.

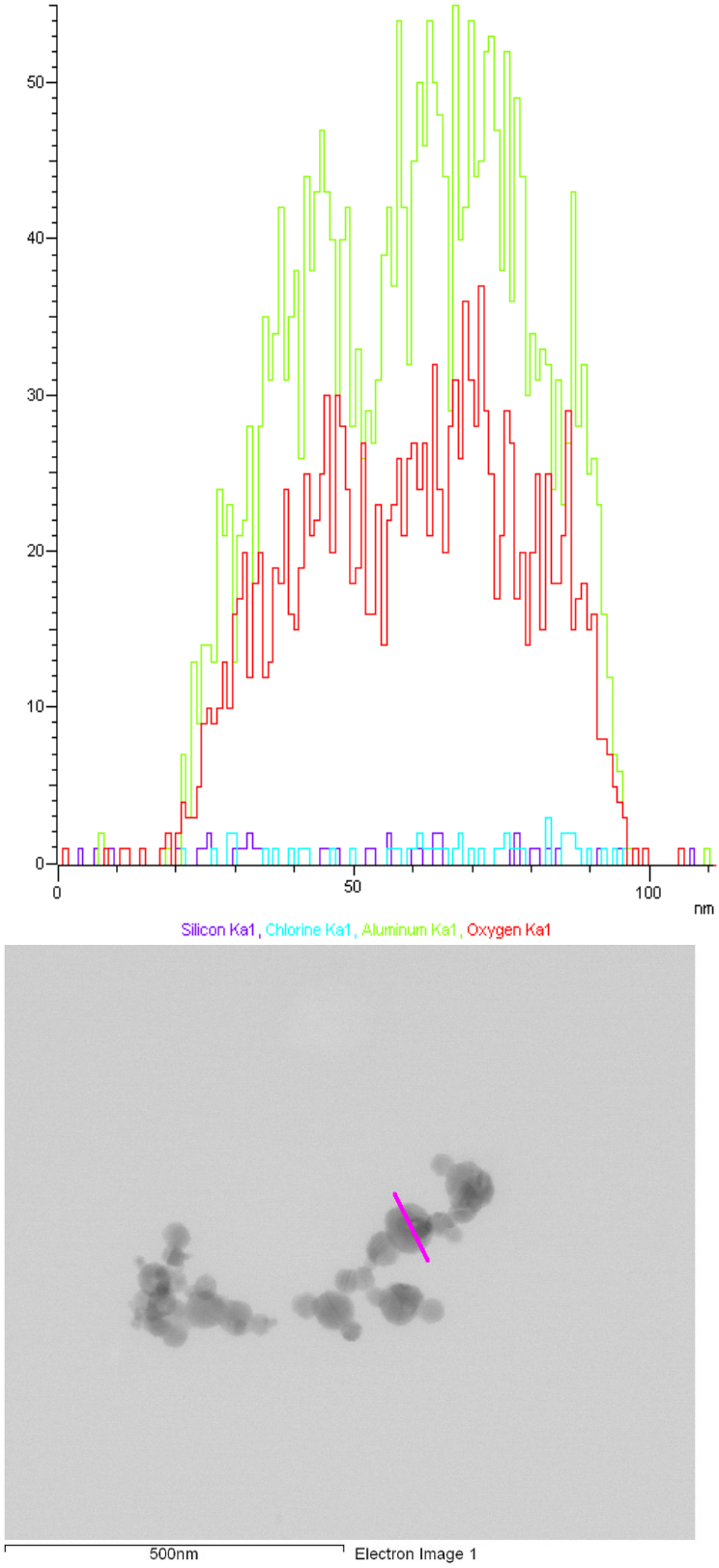

Figure 4-4: EDS data of collected product after exposure to air.

The EDS data reflects the oxidation of the collected $AlCl_3$ particles. Also trace amounts of chlorine (<1%) are detected but not easily seen.

4.4 Thermo-Chemical Calculations of $AlCl_3$

To help understand what went wrong, a more detailed examination into the chemical equilibrium and thermodynamics of $AlCl_3/H_2$ was undertaken. We note two chemical reactions of importance, Formulas 6 and 7. In fact this is how $AlCl_3$ is routinely synthesized. Meaning when creating metallic Al and HCl at high temperatures, at the same time we can react these two products to form back our reactants, $AlCl_3$ and H_2. The chemistry is further complicated by the formation of another stable product AlCl, seen in the two possible synthesis routes [66]:

$$2\ Al + AlCl_{3\ (g)} \leftrightarrow 3\ AlCl_{\ (g)} \qquad (6)$$

$$Al + HCl_{\ (g)} \rightarrow AlCl_{\ (g)} + 1/2H_2 \qquad (7)$$

A chemical/thermodynamic equilibrium investigation of the products in our reactor was explored through the publicly available program CEAqui, Chemical Equilibrium with Applications. CEAqui "is a graphical-user-interface for CEA2, version 2 of NASA Glenn's computer program Chemical Equilibrium with Applications." These thermodynamic libraries are documented in NASA TP-211556, 2002.

Two reactions are run at 1 atm and over the temperatures 100ºC -1900ºC: $AlCl_3$ alone and a molar ratio of 5:1 H_2 to $AlCl_3$ (demonstrating excess hydrogen).

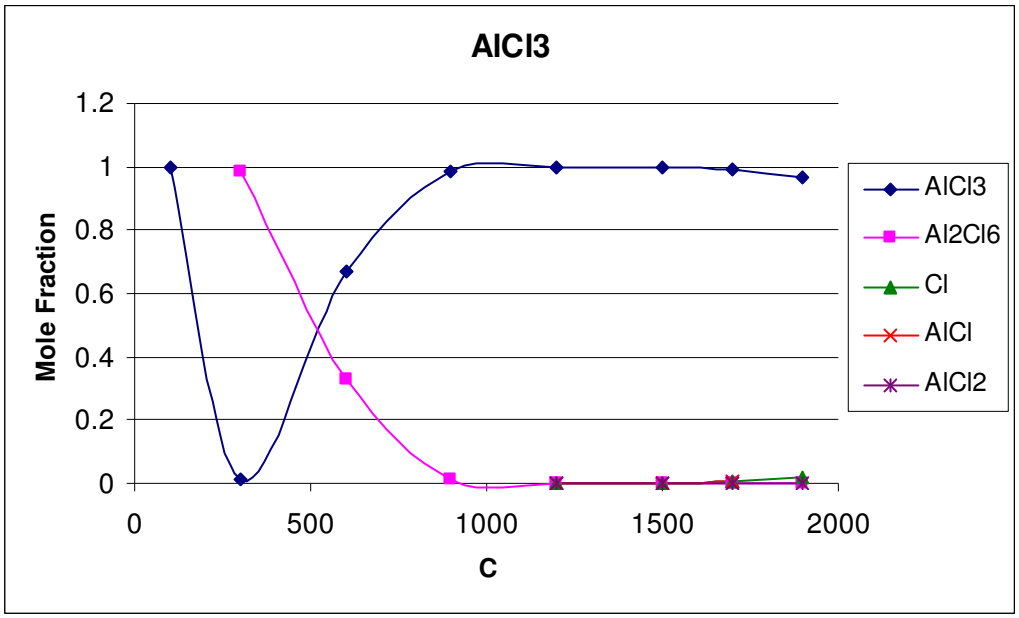

(a)

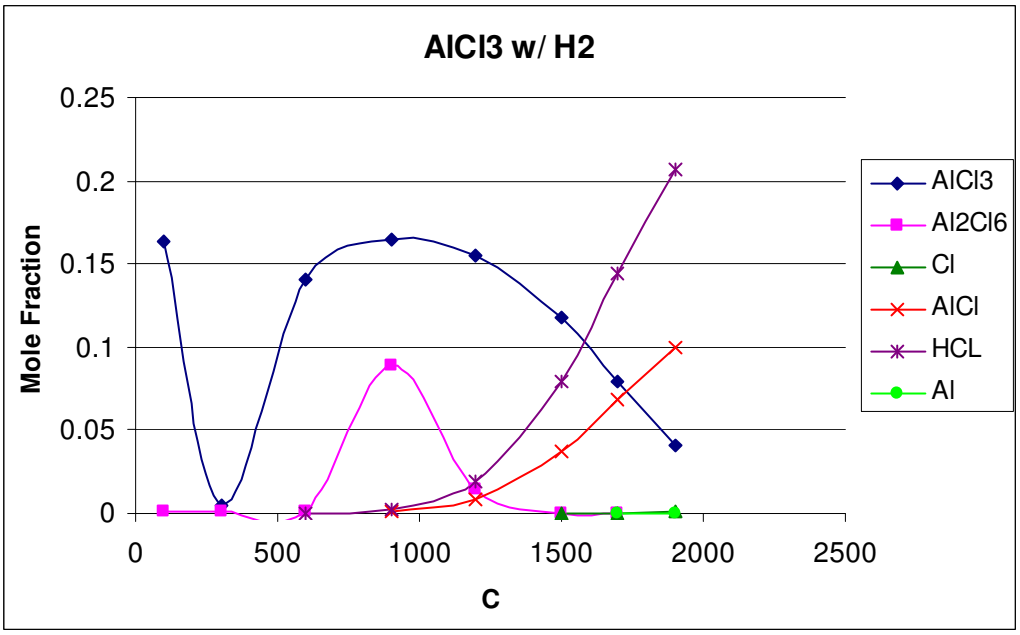

(b)

Figure 4-5: Thermo-chemical calculations of (a) $AlCl_3$, and (b) $AlCl_3$ with excess H_2. H_2 plot is left off (b).

4.4.1 Incomplete Dissociation of $AlCl_3$

The biggest lesson to take way from these calculations is when hydrogen is absent as a reducing agent, no metallic aluminum is formed; the only compounds present are aluminum chloride derivatives. In both simulations, the $AlCl_3$ species is dominant at lower temperatures, becoming significantly diminished at 300ºC, and then the recovering at higher temperatures. The stability of $AlCl_3$ can certainly be questioned at 300ºC, 1 atm.

The formation of HCl at considerable quantities is observed at 1200ºC, the temperature we originally believed $AlCl_3$ would decompose at. HCl formation along with the declining amount of $AlCl_3$ is indicative of partial decomposition. Another positive result of hydrogen is the increased rate at which $AlCl_3$ is consumed when contrasted with no hydrogen. What is most troubling is the increasing quantity of AlCl being formed at higher temperatures especially compared to the relative minute amount of metallic aluminum. Instead of $AlCl_3$, with H_2, completely dissociating to Al and HCl, it favorable forms AlCl and HCl with trace Al and excess H_2.

The plasma technique referenced in Zhang[30] is successful because $AlCl_3$ and AlCl can be completely ionized into its elements and react with the supplied hydrogen, forming HCl and metallic Al [30]. In our experiment the complete dissociation of AlCl is not appreciable. Their plasma reactor is capable of achieving much higher temperatures than our conventional furnaces.

Experimentally the only compounds accumulated are believed to be AlCl and $AlCl_3$. This helps explain our early results and theory that any newly formed aluminum could be quickly reacted with HCl to form back to $AlCl_3$ or AlCl. The formation of AlCl was an unexpected hurdle that chemically can not be accomplished in our current system

with a temperature ceiling of 1600ºC. At the time of these tests, we were unable to increase the temperature of our reactor and produce pristine aluminum nanoparticles.

Chapter 5 Generation, Adaptation, and Characterization of Nickel Particles

In the hope of developing as successful coating process for aerosolized metal nanoparticles for use in a thermite reaction, the focus of my research transitioned from synthesizing aluminum to generating nickel and growing a coating layer on the nanoparticles' surface. The nickel system I used was adopted from Lei Zhou et al [69], another researcher in my group at UMD, College Park.

5.1 Nickel Nanoparticles from Nickel Carbonyl

Nickel was selected partially because we had the materials and capabilities already in place to quickly develop nanoparticles, but also has unique energetic properties described previously. These nanoparticles are generated from a nickel carbonyl precursor. Nickel carbonyl, $Ni(CO)_4$, is thermally decomposed at 420ºC, in which Ni and CO are produced in three abstraction steps[36];

$$Ni(CO)_4 \rightarrow Ni(CO)_3 + CO \quad (8)$$

$$Ni(CO)_3 \rightarrow Ni(CO)_2 + CO$$

$$Ni(CO)_2 \rightarrow Ni + 2CO$$

Metal carbonyls in general are very toxic and must be handled appropriately. This risk is magnified given it is aerosolized with the potential to breathe it in [53]. To mitigate some of the hazard, we generated and destroyed the nickel carbonyl in-situ with our system. A packed bed of nickel powder (3 micron, 99.7% purity, Sigma Aldrich), is fed with carbon monoxide (99.5%, Airgas). The bed is held at 50ºC by heating tapes. The

reaction is the reverse of that posed in Reaction 8. To ensure that surface of nickel powder is clean, hydrogen (99.5%) is passed in lieu of carbon monoxide to the nickel bed, now heated to 350ºC by same heating tapes. This cleaning process occurs for no less than four hours and can usually be done overnight, and should be conducted before each run[69].

At the end of the bed, the nickel carbonyl is mixed with a carrier flow of argon (industrial grade, Airgas). The flow is directed to two quartz tubes in the first furnace set at a decomposition temperature of 420ºC. While one of the tubes directs the particles to the rest of our system, the other flows to exhaust. Prior to decomposition of the usable particles, they are mixed with an addition dilution flow of argon. The dilution flow is approximately one order magnitude less than the carrier flow.

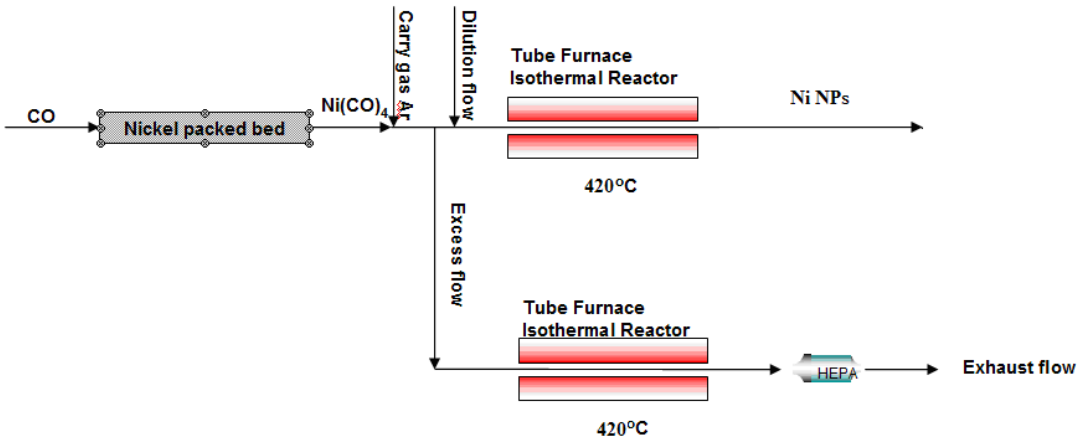

Figure 5-1: Diagram of nickel nanoparticle synthesis. Adopted from L. Zhou[69].

5.2 Particle Formation

The synthesis of the nanoparticles initiates as the aerosol (Ar+CO+Ni) leaves the hottest region of the cracking furnace, cooling and condensing. The atomic/small clusters

of nickel begin to crash into each other and nucleate out. From here, surface growth of nickel dominates and nanoparticles are formed. These particles have been shown to be highly agglomerated, comprised of a primary size less than 10nm [69]. With the notion that we want to coat particles, these agglomerates are not ideal.

The aerosol is passed through a sintering furnace at 1100ºC to produce larger primary particle sizes and suppress agglomeration. It is prior to this sintering that we exhaust 80-90 % of our particles. Having too high of a concentration can cause problems with accurate measurements and long term health of the system/equipment. The CPC also has a limit as to the maximum number concentration of particles it can count. We risk miss counting our data, failing to read above 1 x 10^9 # particles/cc. From preliminarily data collected after a 90% dump, we can observe total concentrations up to 1.10 x10^8 # particles/cc; justifying the decision to exhaust most of our flow immediately. Ideal flow rates were determined to be:

- Ar for dilution: 385 sccm,
- Ar as main carrier gas: 2150 sccm
- CO for $Ni(CO)_4$ generation: 60 sccm,
- H_2 for cleaning nickel bed: 60sccm.

5.2.1 Actual and Theoretical Production Numbers

Because the exhaust is passive, no vacuum, its percentage is based off our total supplied gases and the sampling flow rate of our equipment. Total flow rate of argon and carbon monoxide is ~2.5 lpm, while flow rate to DMA/CPC is 0.3 lpm and TEM electrostatic collector pulls 0.5 lpm. Knowing this we can back out our current and theoretical maximum mass per unit volume, to at least order of magnitude

approximations. Sampling with the DMA/CPC (.3lpm) at these flow rates, yields an average of 1.89 x10^4 micrograms per m^3. Over a ninety second sample, we produce a usable 8.505 micrograms of nickel or 255 micrograms per hour. If we had not partially exhausted the system, the total amount generated would be ten times this amount: 2550 micrograms per hour.

5.3 SMPS Analysis

DMA/CPC data shows over various runs, a geometric mean mobility diameter range of 53 to 62 nm. Concentrations in these trials remain consistent and on the order of 1 x10^8 # particles/cc. A sample size distribution of the nickel nanoparticles generation is presented in Figure 5-2.

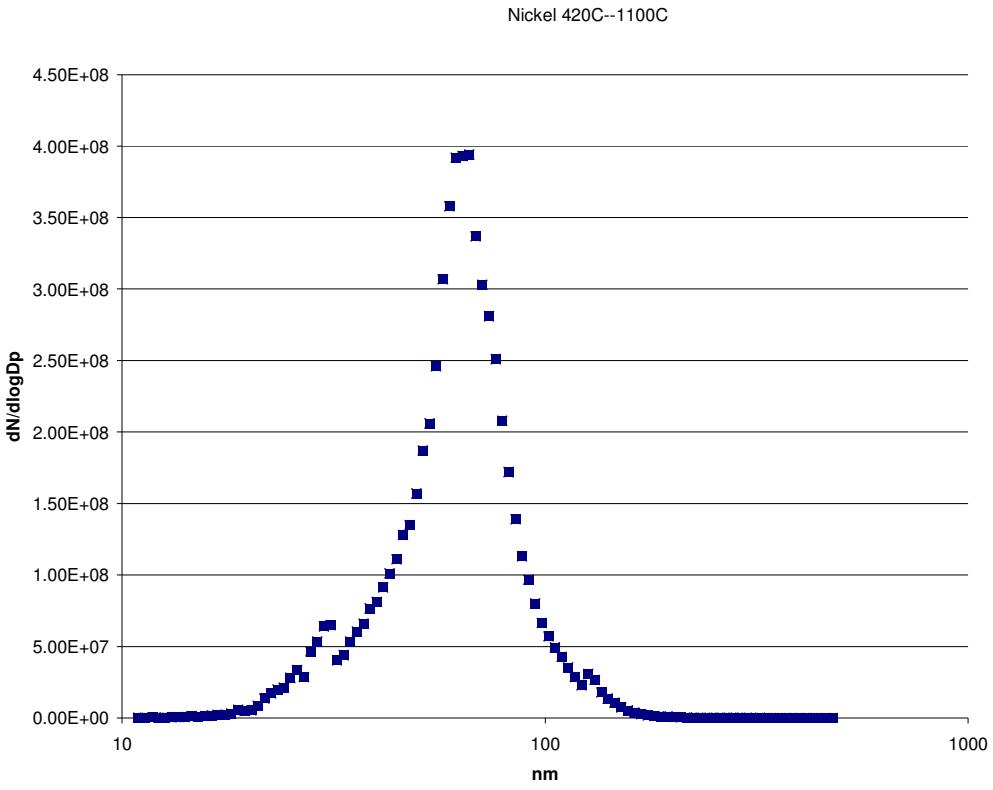

Figure 5-2: Size distribution of Nickel nanoparticles run through decomposition and sintering furnace.

5.4 HRTEM Analysis

Particles for TEM analysis were collected on a TSI Electrostatic Aerosol Sampler for 20 minutes trying to match the flow rate of the DMA/CPC system (0.3lpm); the actually flow rate ranges from 0.3 to 0.5 lpm. Grids used are Ted Pella copper with a Formvar support.

The same TEM microscope is used in the aluminum investigation described in Chapters 3 and 4. Below, pictures show a mix of individual nickel particles, small and large chain-like agglomerates. These linear/chain agglomerates are common to magnetic nanoparticles[70]. HRTEM reveals that smaller nickel nanoparticles (less than 25nm) appear to be single crystalline. This is expected since we are sintering at 1100ºC[71].

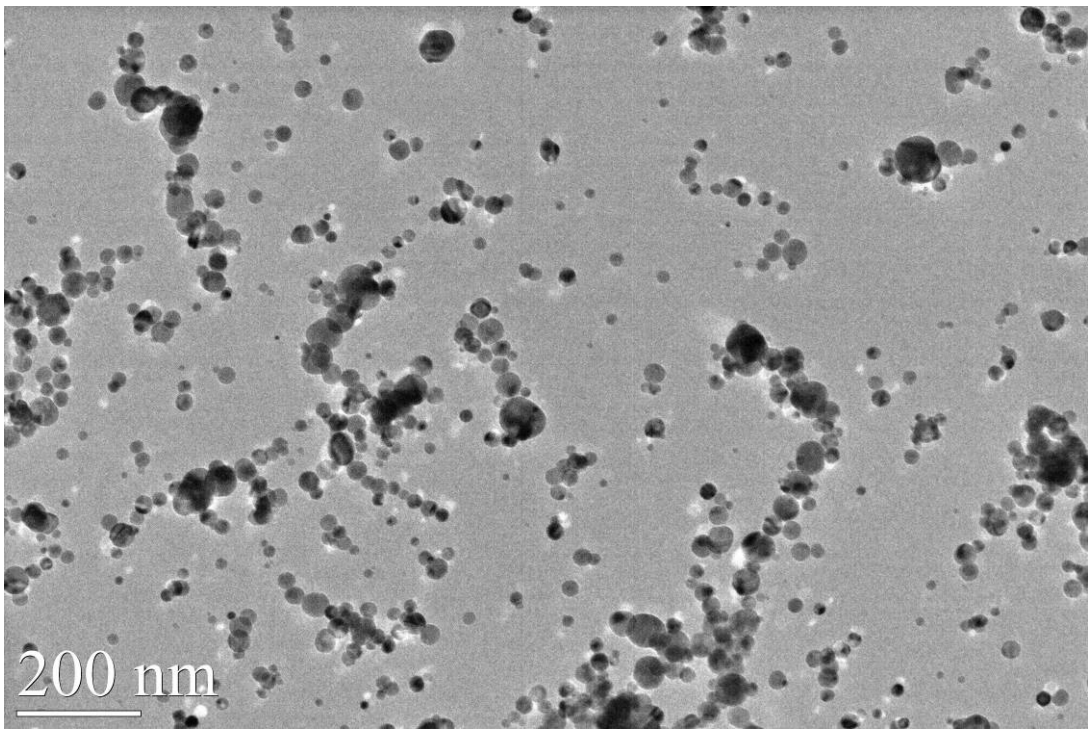

Figure 5-3: TEM image of nickel nanoparticles.

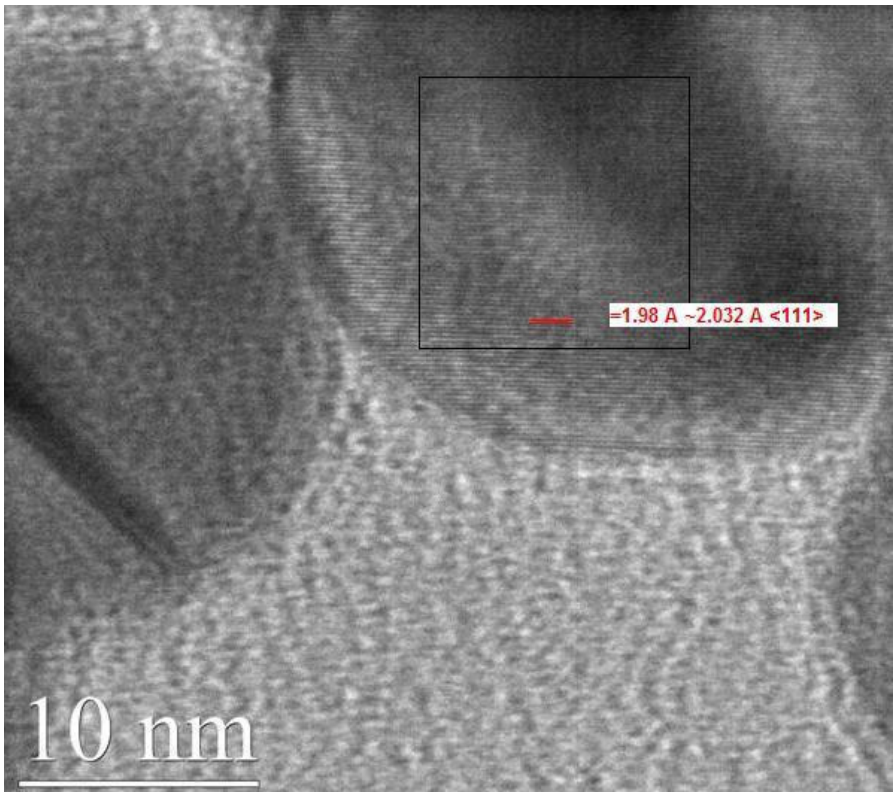

Figure 5-4: HRTEM image of a single crystal nickel nanoparticle.

A lattice spacing of 1.98 angstroms is measured corresponding to a <111> crystalline direction. The HRTEM pictures also confirmed the nickel particles have little or no real observable oxide shell. This will be important later when we observe a much thicker shell on our particles. A similar effect is observed by Zhou et al when oxidizing nickel at temps less than 200ºC [69]. We note that when looking at the HRTEM image above, where crystallinity ends at particle's surface, an oxide layer less than 1nm (monolayer or two) could exist. But this can not be extensively concluded. The oxidization of our particle, if it occurs, would take place when exposing our TEM grid to air at room temperature. TEM analysis was carried out within 24-48 hours of synthesis.

Chapter 6 Iron Pentacarbonyl Background

Iron pentacarbonyl, sourced from Sigma Aldrich, serves as our precursor for iron. Given our aerosol of well characterized nickel nanoparticles, we wish to apply a coating of iron, and ultimately iron oxide, to nickel's surface. This precursor, like most carbonyls', is toxic and must be safely handled. Unlike nickel carbonyl, which is created in the gas phase, iron carbonyl is purchased as a liquid and then vaporized for our aerosol work. A system for the growing of iron/iron oxide onto nickel nanoparticles and their subsequent in situ characterization is diagramed in Figure 6-1 below.

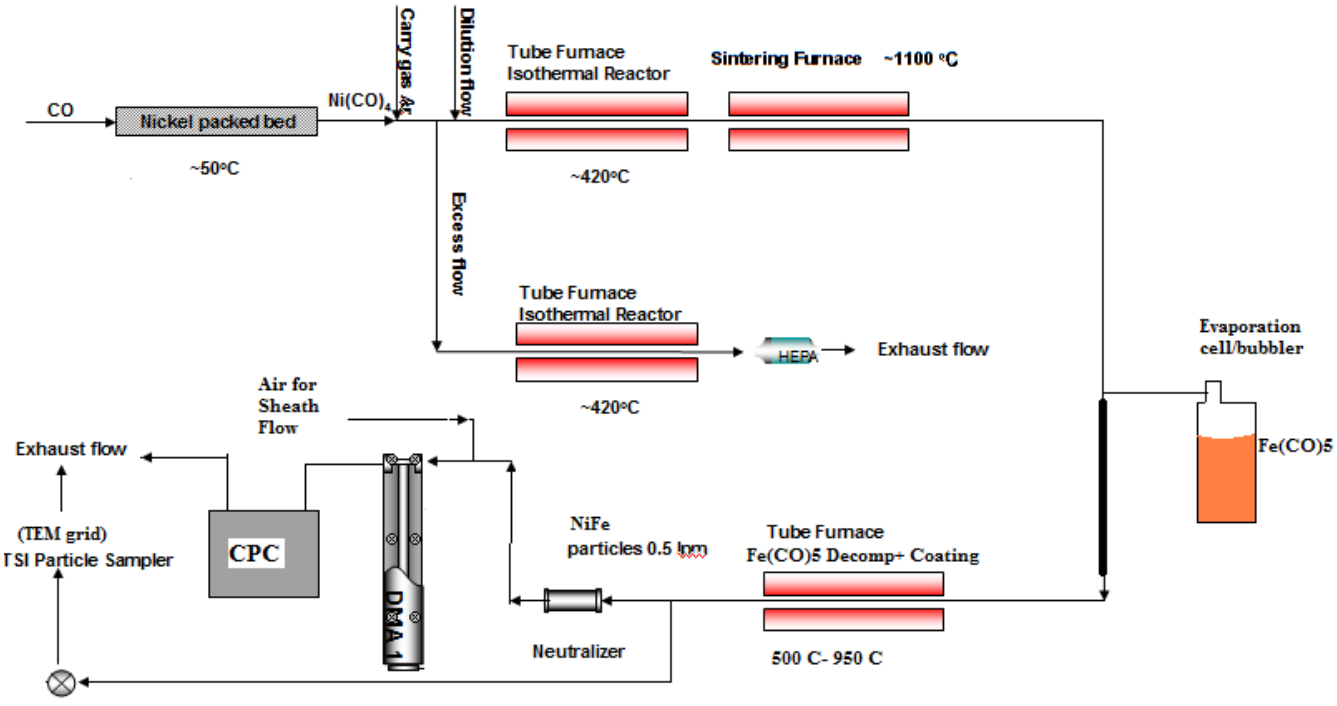

Figure 6-1: Diagram of our combined nickel reactor and iron coating system.

Nickel and iron carbonyl also share fundamental decomposition reactions[58; 72]:

$Fe(CO)_5 \rightarrow Fe(CO)_4 + CO$ (9)

$Fe(CO)_4 \rightarrow Fe(CO)_3 + CO$

$Fe(CO)_3 \rightarrow Fe(CO)_2 + CO$

$Fe(CO)_2 \rightarrow Fe(CO) + CO$

$Fe(CO) \rightarrow Fe + CO$

We observe that this precursor does not behave as straightforward as one would expect. Tepe et al thermally decomposed iron carbonyl over a temperature range of 20ºC to 180ºC and measured CO with IR absorption cells[58; 60]. They state the decomposition begins at 50ºC. While Karlsson et al stated incomplete decomposition up to 250ºC[60]. From our experience we have also seen the precursor breakdown upon exposure to light. We start our experiments at 950ºC to ensure that the iron carbonyl is completely decomposed and investigate this with the DMA/CPC. It is the favorable bond energies of Fe-C and C≡O that allow for the successful use of iron carbonyl as an iron precursor. But we must carefully monitor for any generation of solid carbon, as a result of the Boudouard reaction and the catalytic nature of iron nanoparticles[73].

$CO \rightarrow CO_2 + C(s)$ (10)

6.1 Bubbler vs. Evaporation Cell: Vapor Pressure Troubles

The difficulty in using iron carbonyl is controlling the amount of material we wish to vaporize into an aerosol. A glass bubbler filled with 25ml of iron carbonyl is connected to an outlet that feeds a tube furnace. Argon is supplied by the MKS flow unit.

For the initial tests bubbler flow is set at 39.5 sccm (the lowest our current flow unit can stably provide) with a furnace temperature of 950ºC.

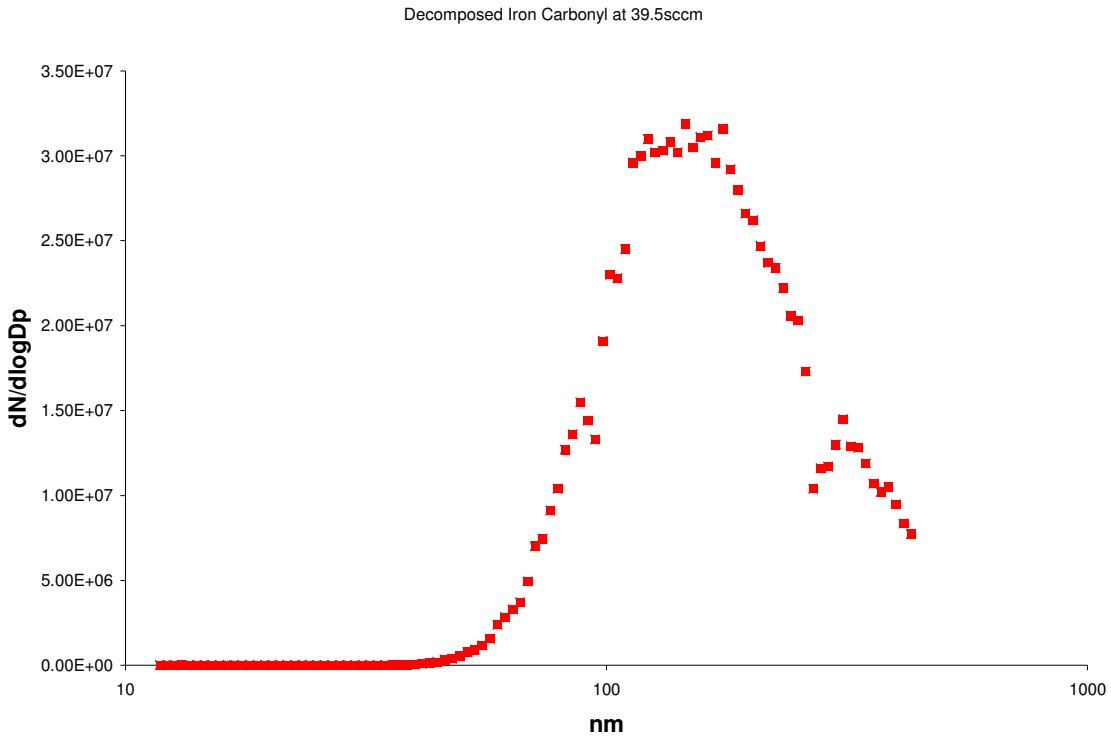

Figure 6-2: Size distribution of bubbling iron carbonyl at 39.5sccm

The TSI software, Aerosol Instrument Manager, supplied with the SMPS system, calculates the mean mobility diameter to be 161.7 nm with a total concentration of 1.61 x10^7 #particles/cc. It is immediately clear that this would not be a good coating; it is a larger and potentially more concentrated distribution than our nickel. A larger concentration is indicative that the iron is homogenously nucleating too quickly and at too large a scale. Surface growth continues with the ample supply of iron and the particle swells to the peak diameter. Homogenous nucleation of the iron is bad for our coating process because instead of growing on a nucleation surface site on a host/core particle, the iron simply crashes out, leaving a separate mix of iron and nickel particles. Why at

such a low flow rate does the system produce so much iron and how can we address it, while suppressing iron nucleation?

This is not the first time this behavior has been observed for iron carbonyl. In the process of generating a monodisperse-like distribution of 20nm iron nanoparticles for silicon nanowire growth, Karlsson et al show very similar characteristics[60]. When flowing 10 sccm argon over the precursor, a short and wide distribution is obtained. To obtain their desired particles, no flow is allowed into the chamber; the supply of iron carbonyl is control purely by evaporation off the surface and diffusion into the lines with a carrier gas. A nice narrow distribution peaking at ~20nm, is observed.

We have adopted a comparable approach, since the goals of our research our similar. While we are attempting to avoid nucleation of iron, we require only a small amount of material remaining in gas phase to mix with our aerosolized nickel. These two requisites fit well together; the lower the concentration (lower mass), the less homogenous nucleation occurs, holding everything else constant. For the rest our experiments the flow to the bubbler is removed and the evaporation/diffusion technique is employed. The SMPS is once again used to probe the distribution at evaporation conditions.

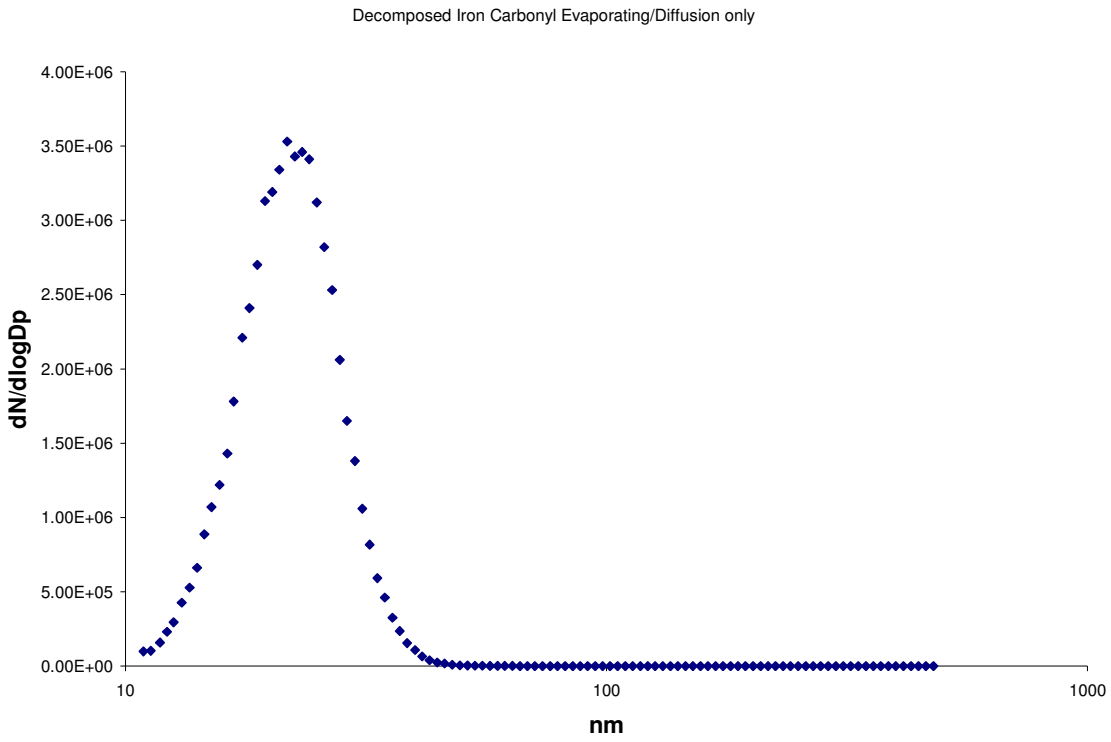

Figure 6-3: Size distribution of evaporating iron carbonyl (no flow).

A geometric mean mobility diameter is observed at 21.7 nm and a total concentration of 8.94 x10^5 #particles/cc. The comparison between the two setups is stunning and surprisingly matches qualitatively well to the Karlsson et al data[60]. Both samples ran at decomposition furnace temperature of 950ºC.

6.2 Probing Iron Pentacarbonyl Decomposition

To determine the effect the decomposition temperature has on the size distribution, a range of 150ºC to 850ºC was explored. We also hoped to identify any critical temperatures. Our results are displayed in Figure 6-4 below.

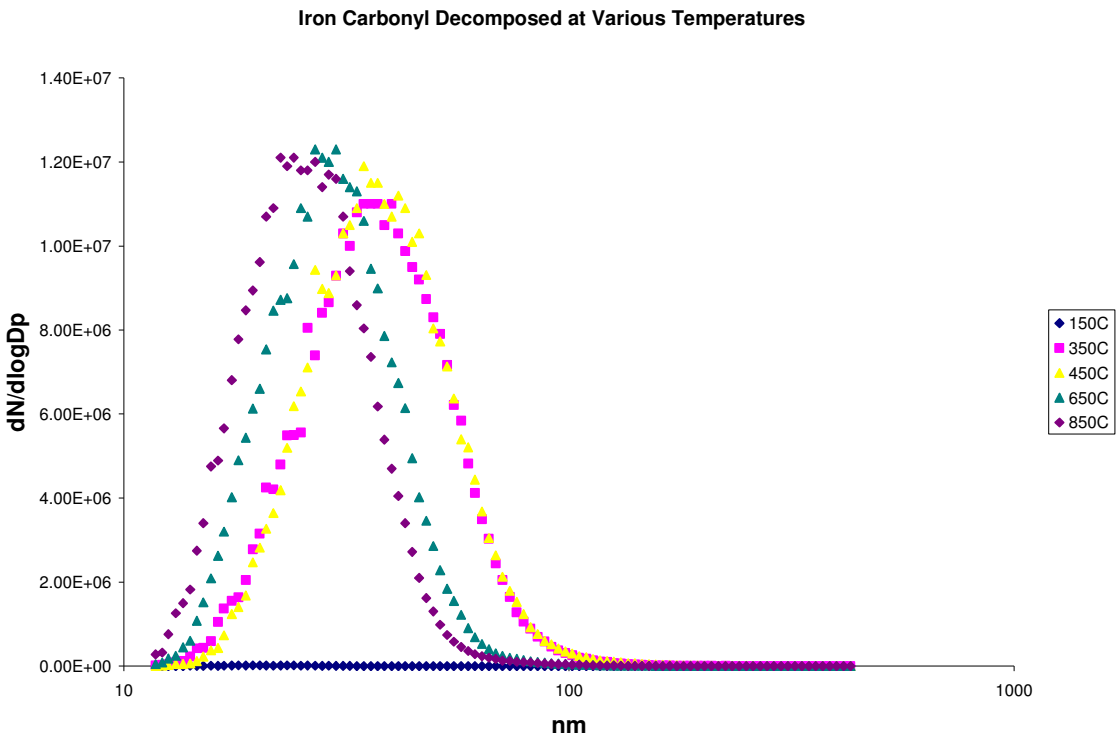

Figure 6-4: Size distributions of iron pentacarbonyl decomposition at various temperatures.

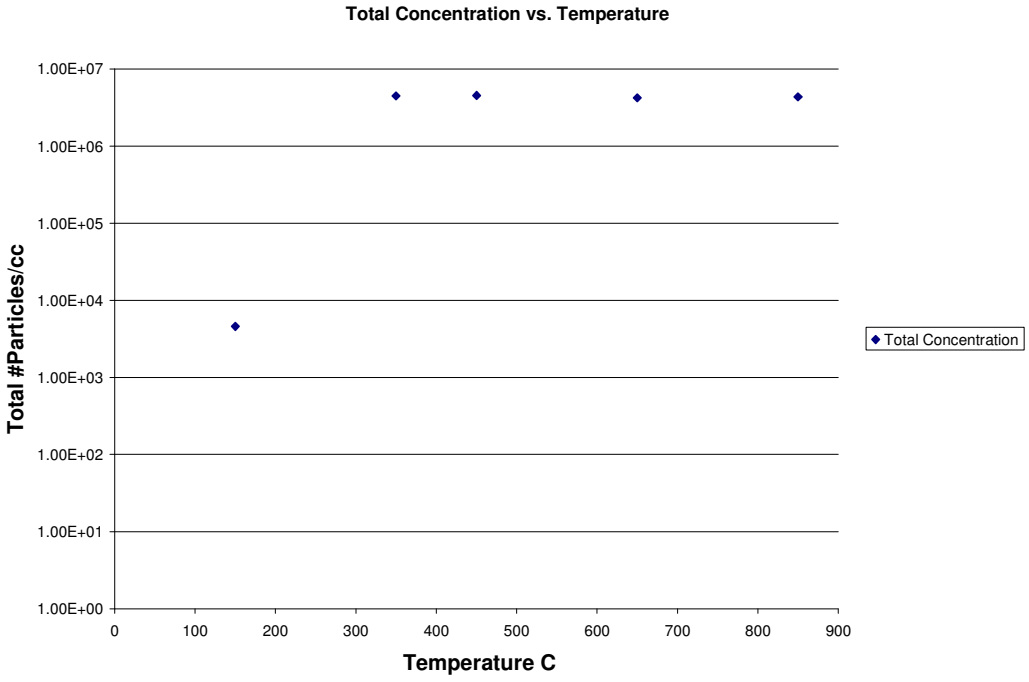

Figure 6-5: Total concentration of iron aerosols at various decomposition temperatures.

Below temperatures of 350ºC, the distribution is jagged with concentrations around 4 $x10^3$ #particles/cc. At 150ºC, shown in dark blue, the sample does not fit on scale with the rest of data, but has an average mobility diameter similar to 350ºC. Sampling at 350ºC, the concentration is observed to jump dramatically to 4 $x10^6$ #particles/cc, as seen in Figure 6-5. This is a 1000x greater. Exploring temperatures regions up to 850ºC yield total concentrations that never exceed ~8 $x10^6$ #particles/cc. It is theorized that above 350ºC the majority of our iron carbonyl is completely decomposed. This provides a lower limit on which conditions are optimal for coating.

It is safe to assume that the evaporation of iron does not change in the time period of this experiment, or at least not enough to cause such a magnitude change from 150ºC to 350ºC. We attribute this increase in concentration of iron particles to the increase in the decomposition of iron carbonyl. Remember, the decomposition of iron carbonyl is believed to only start at 50ºC and is a series of five reactions.

6.2.1 Predicting Dramatic Jump in Particle Count

To explain and even predict this large jump in particle concentration we look at the decomposition rate of iron carbonyl. We will use the adjusted rate,

$$K= 1.5 \times 10^{12} \exp(-10060.14/T)\ cm^3\ mole^{-1}\ s^{-1} \qquad (11)$$

originally described by Rosenberg and Wray, but presented by Biswas et al[74]. In Biswas et al, the pre exponent factor has been reduced by $1/40^{th}$ for closer fit with their simulations. From this rate we can get order of magnitude changes in decomposition rates at various temperatures.

T (ºC)	K_{Fe} ($cm^3 mole^{-1} s^{-1}$)
50	4.46×10^{-2}
150	7.03×10^{1}
250	6.64×10^{3}
350	1.45×10^{5}
450	1.36×10^{6}
550	7.37×10^{6}
650	2.77×10^{7}
750	8.04×10^{7}
850	1.93×10^{8}

Table 6-1: Coefficient of iron pentacarbonyl decomposition rate at various temperatures

We pay special consideration to the values at 50º, 150º and 350 ºC. At 50º C precursor decomposition is low, in good agreement with our understanding that it is just beginning to crack.. What is useful for our investigation is the change in rate from 150º to 350º C. The ratio of K_{Fe}(150º C) to K_{Fe}(350º C),

$$1.45 \times 10^{5} / 7.03 \times 10^{1} = 2.06 \times 10^{3}$$

, and the ratio of our experimental particle concentrations at 350º C and 150 ºC, respectively,

$$4 \times 10^{6} / 4 \times 10^{3} = 1 \times 10^{3}.$$

In a consistent volume and time, this is in good agreement with our thousand fold increase in particles concentration, providing credence to our belief that the increase in particle concentration is due to an increase in iron carbonyl decomposition. Simply stated,

at 350 ºC we have an order of a thousand times more iron in our system to form particles with. Following the table above, we would then expect concentration to increase at higher temperatures, but experimentally this is not observed. Remember, that these values are predicted rates and our system is defined by a constrained amount of iron carbonyl. We believe that the decomposition rate above 350ºC is sufficient to fully decompose the amount of iron carbonyl introduced to the furnace. We see later that when trying to coat at high temperatures the decomposition chemistry takes place too quickly and the coating fails; the iron homogenous nucleates out.

Of note Figure 6-4 confirms the compaction of iron particles at increasing temperatures, also observed by Karlsson et al[60].

Chapter 7 Surface Coating of Nickel Nanoparticles with Iron Oxide

Evaporated iron carbonyl is combined with the carrier flow of argon and our nickel nanoparticles. The two flows mix and pass through two regions; a room temperature shielded Tygon tube to prevent light from prematurely cracking the iron carbonyl and a quartz furnace tube where controlled decomposition takes place. The residence times in our coating system are as follows:

- $Ni(CO)_4$ decomposition- 5 sec
- Ni sintering- 5 sec
- Shielded Tygon mixing zone- 7.2 sec
- $Fe(CO)_5$ decomposition- 26 sec

When originally designed, we had planned on cooling the precursor with ice and salt when bubbling argon, but abandoned the idea when the argon flow produced too much iron. The evaporation now takes place at room temperature (17ºC-20ºC), but we have the capability to heat the solution with heating tapes.

7.1 Procedure and First Attempts

As described before, the basic procedure for coating is: create the nickel aerosol, take a SMPS reading of size distribution, open the valve to evaporation chamber of iron carbonyl, feed mixed aerosol(s) to decomposition furnace and take another size distribution of final product aerosol.

In our first coating attempt we ran a bubbler flow 39.5 sccm and cooled bubbler with salt ice water (-6ºC). As expected iron dominates our product and on TEM/EDS completely masks any nickel. So much so that almost no nickel is observed in an elemental analysis.

Our second coating attempt corrects for the abundance of iron by transitioning to the evaporation technique. With a decomposition furnace at 950ºC, no noticeable increase in host particle size is observed. Ideally, a coated nickel particle would show a shift (rightward) in size distribution with a consistent concentration.

TEM images of this particle show a similar agglomeration of the host nickel with no coating or surface growth. What is observed is the partial sintering of the nickel occurring in our decomposition furnace. In the same experiment, the nickel bed is turned off at end, leaving just evaporation of iron carbonyl and carrier flow on.

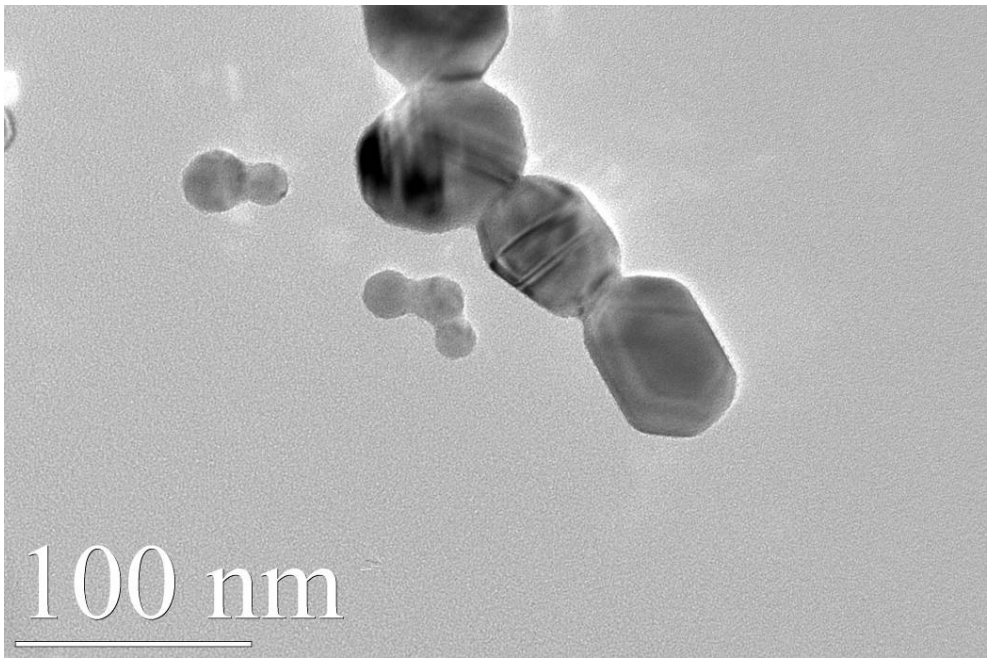

Figure 7-1: TEM image of partial sintered bare nickel nanoparticles at decomposition temperature of 950ºC

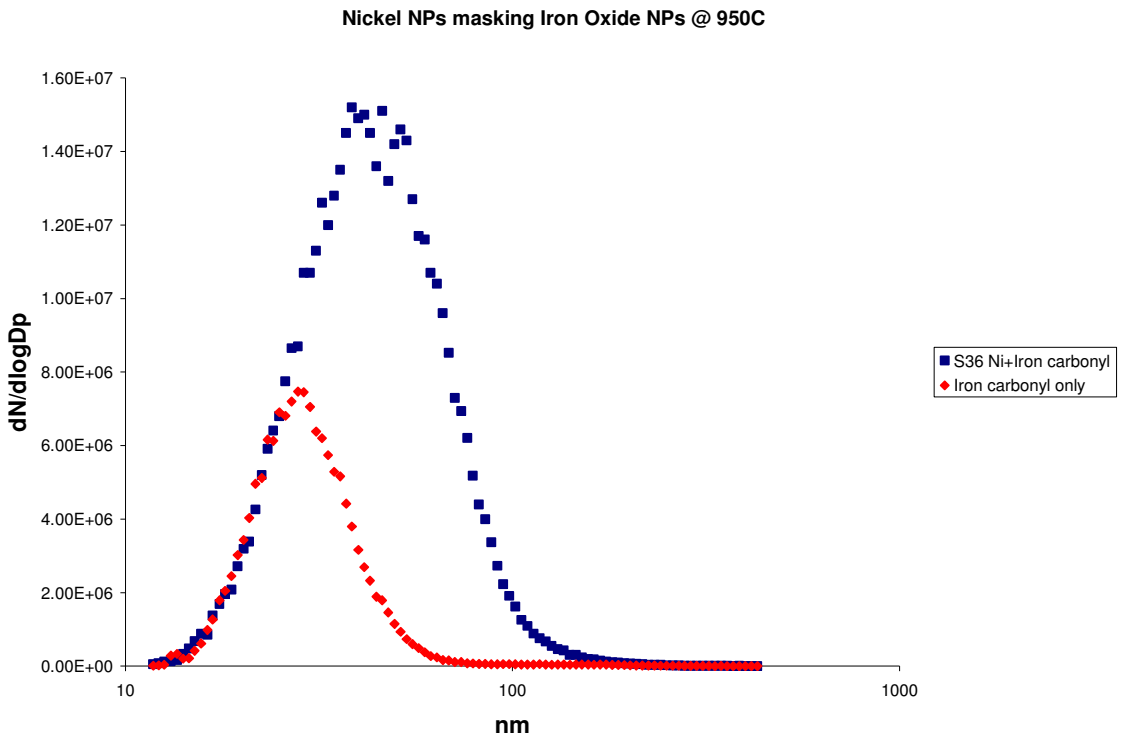

Figure 7-2: Masking of iron oxide by nickel size distributions.

The peak of iron is clearly evident at ~27nm and peak of nickel is ~47nm. The concentration of the iron is mostly being masked by the nickel concentration.

This is a puzzling behavior since the mass of iron we are producing is ideal for putting a sufficient coating of iron on nickel's surface. We believe because of our high temperatures and profile of the furnace, the decomposition of iron carbonyl and particle formation is happening too readily; homogenous nucleation and subsequent surface growth of iron on iron. Essentially the chemistry of the system is too fast. Because it has proven difficult to control the amount of iron carbonyl we can introduce to our system, we opt not to add more. If we did this we risk increasing the rate of nucleation and size of iron particles, rather than adding it to a surface coating of iron.

7.2 Successful Coating with a Lowered Furnace Temperature

In our next attempt, the furnace temperature was lowered to slow the reaction chemistry down. By extending the time of decomposition, we reduce the amount of iron present in the flow at a given time and volume. This reduced concentration helps suppress homogenous nucleation and the presence of nickel particles tilts the favorable pathway towards surface growth, our coating mechanism; the nickel particles supply nucleation surface sites for the decomposed iron. Similar to the previous runs, a size distribution of nickel is collected first. Then the valve to the evaporating iron carbonyl is opened. The flows of the system remain the same as before; the bubbler temperature is run at room temperature (~17-20ºC) and the furnace operates at 500ºC. After several runs a consistent increase in size is observed. All further tests are run with the iron carbonyl decomposition furnace at 500ºC.

An average nickel geometric mean diameter of ~65nm is recorded over several runs and after immediately opening the evaporation valve, the diameter jumps. An average value of ~72nm is observed for the final particle size.

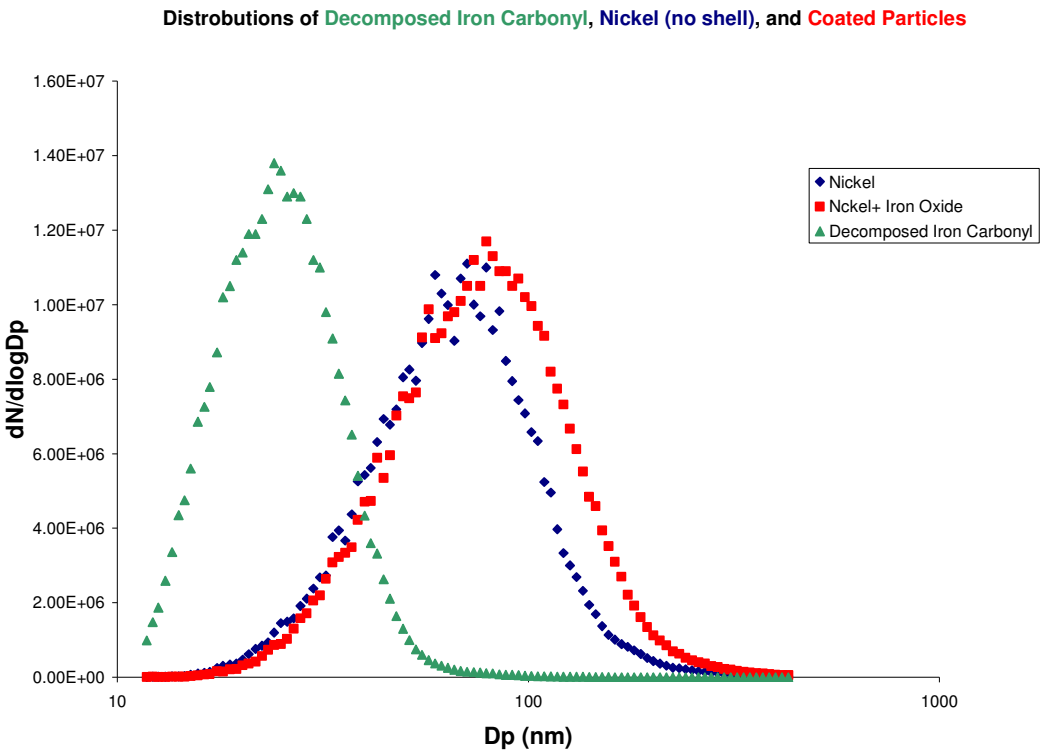

Figure 7-3: Particle size distributions for iron (green), bare nickel (blue), and iron oxide coated nickel (red).

Observed shift in peak.

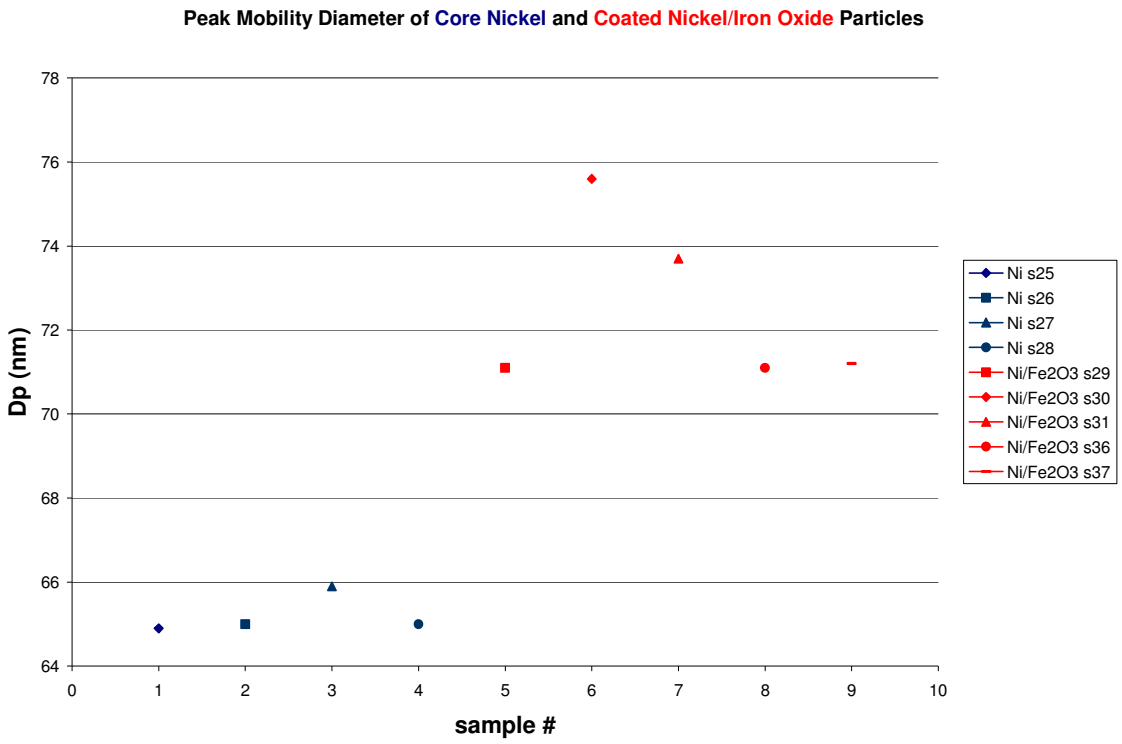

Figure 7-4: Peak Mobility diameters of bare nickel and coated nickel nanoparticles.

This clear and rapid increase in size is not observed with nickel alone; adding further evidence that the iron is interacting with the core nickel particles. Studying the approximate volume of particles in the aerosol (Figure 7-3) for iron, nickel and iron oxide coated nickel, reveals the volume change from nickel to iron oxide coated nickel is on the same order as the volume of the iron particles alone. We attribute the expansion of particles to a surface growth of iron/iron oxide on nickel.

7.2.1 Proposed Growth of Shell Coating

The proposed synthesis is as follows; already formed nickel nanoparticles/agglomerates, carried by argon, mix with iron carbonyl for approximately seven seconds. This mixing region is light shielded to prevent premature decomposition. When the aerosol enters the temperature profile of the furnace it immediately begins the

decomposition described by Reaction 9. As atomic iron is formed, two pathways are possible and are likely to occur concurrently. Iron atoms diffuse directly to the nickel particles/agglomerations, and iron atoms diffuse toward other iron atoms (homogenous nucleation) to form clusters which impact and stick to the larger nickel particles/agglomerations. Layers of iron build over nickel. It is at this point that we have coated our nickel in iron. The pristine iron coating only lasts until we sample the particles with the DMA/CPC or collect on a TEM grid exposed to air. In both processes the iron is rapidly exposed to ambient air conditions, transforming to iron oxide.

Currently we only study the oxidized state of our particles' surface. From an energetics standpoint, this is advantageous because we have deposited an oxidizer on top of a metal fuel. It is important to note that nickel/iron oxide is not a thermite; nickel serves a place holder for other favorable metal fuels. Given a similar size and concentration of said metal fuel particles, an analogous coating of iron oxide would be generated. The coating here is a physical process, meaning there is little or no chemical reaction between the nickel surface and iron/iron oxide that promotes it surface growth. Future research is needed to study the substitution of a more appropriate metal as a core material.

7.3 Coating Characterization

7.3.1 TEM

For confirmation of our iron oxide coating, TEM and EDS analysis is carried out with 48 hours of generation. During this time the samples rest in ambient air, further significant oxidation is not expected to occur given the time period, previous oxide layer

thickness and room temperatures[13-15]. A core-shell structure is clearly evident in the TEM pictures below. HRTEM images reveal the thickness of the coating and polycrystalline nature. The shells show lighter contrast in the TEM, a sign of an oxide. The thickness of the shell averages ~5nm over various sizes of core nickel. Of the particles observed the overall diameter mean is around 30-40nm.

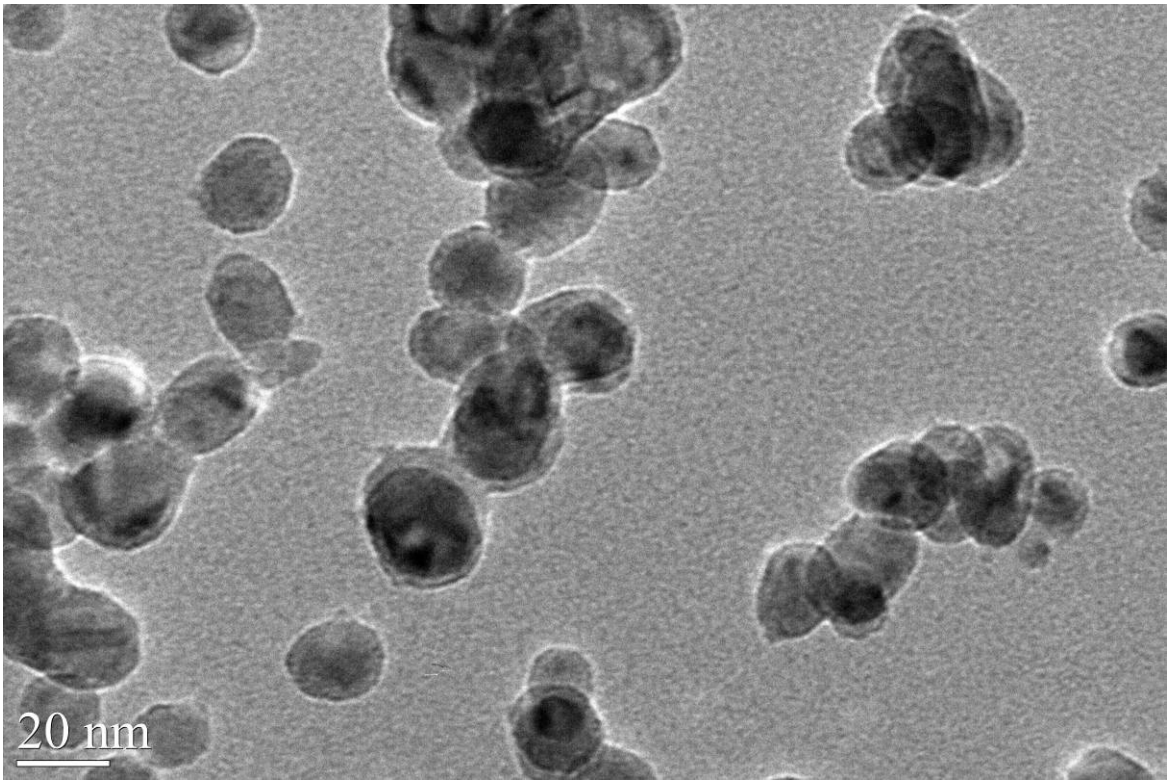

(a)

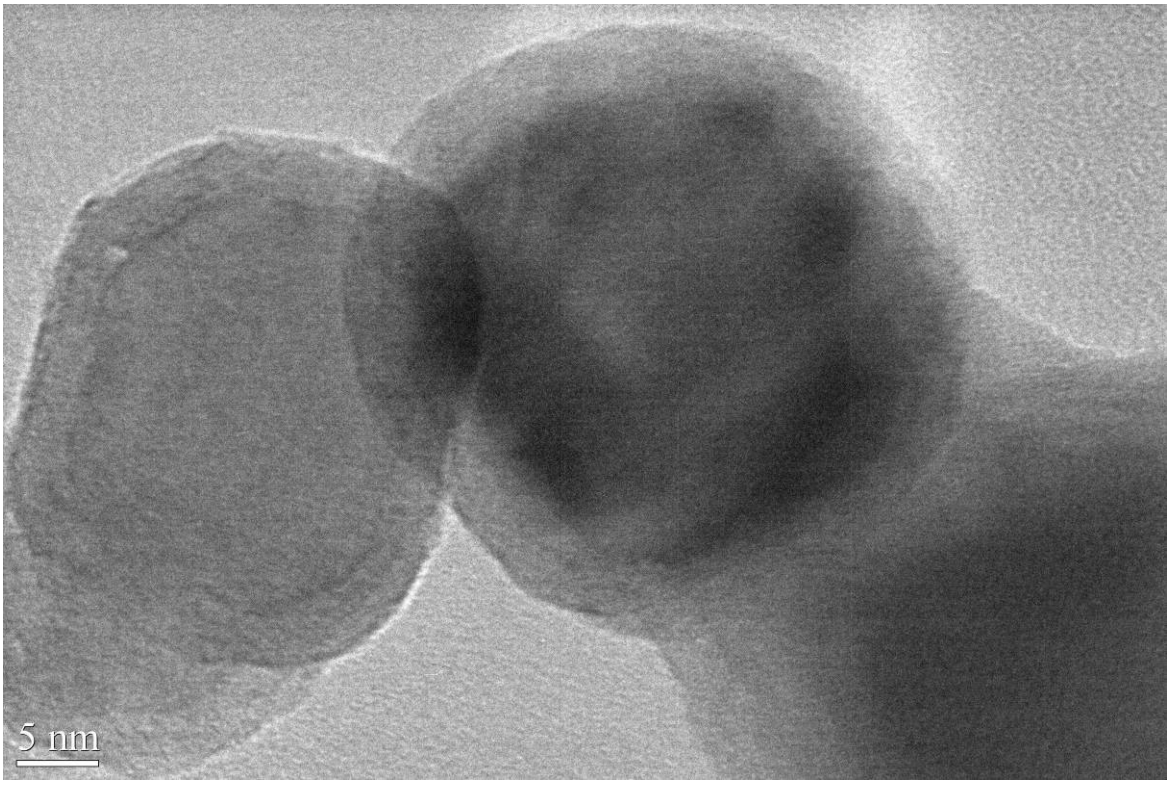

(b)

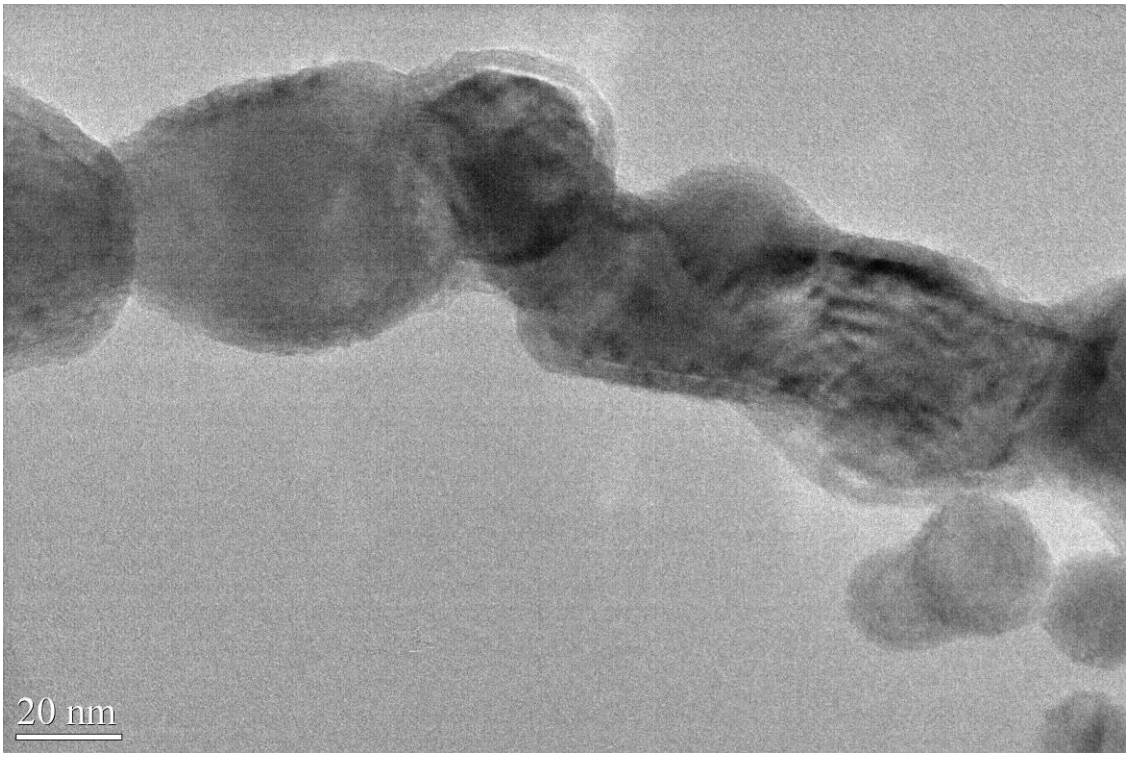

(c)

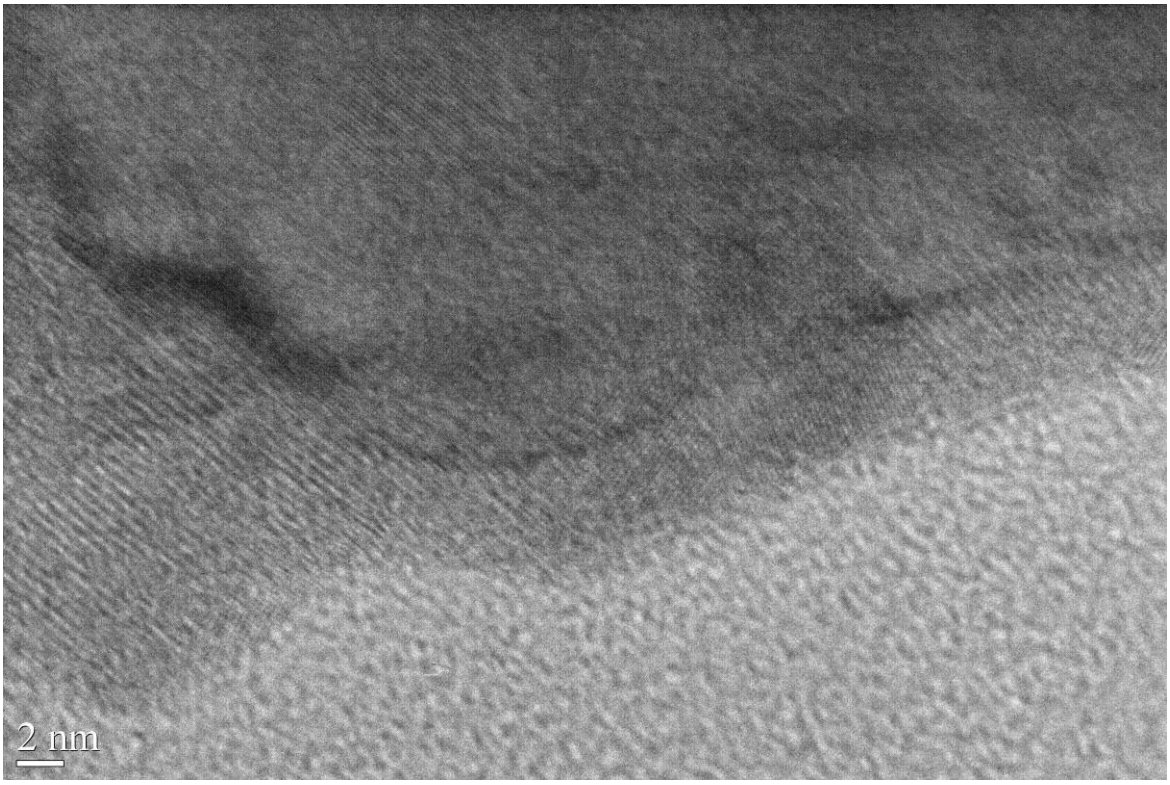

(d)

Figure 7-5: (a-d) TEM images of coated nanoparticles @500ºC.

The discrepancy between the DMA and the TEM is expected. The DMA system measures particles size by balancing the electrostatic/Columbic force and drag force. Drag force is a function of surface area, and assuming a spherical particle would be a function of only diameter. But because our nickel/iron particles are agglomerated, the system will inflate the mobility size of the aerosol. It is interesting that that change in size, thickness of the iron oxide shell, is measured fairly well by the SMPS; an average increase of ~6nm, compared to TEM measurements of ~5nm.

7.3.2 EDS and Polycrystalline SAED

EDS of the sample shows a composition of Ni, Fe and O (excluding background of Cu and C from grid). The explicit observation of only Fe and O (exclusion of Ni) in

the shell is not observable given the drift of sample in the microscope. A site-locking feature is used but its error is greater than the size of the Fe-O layer. In a qualitative assessment Fe-O is observed over a particles' surface, considering that the shell of Fe-O exist in three dimension and we are sample in two; the three dimensional composition is projected in two.

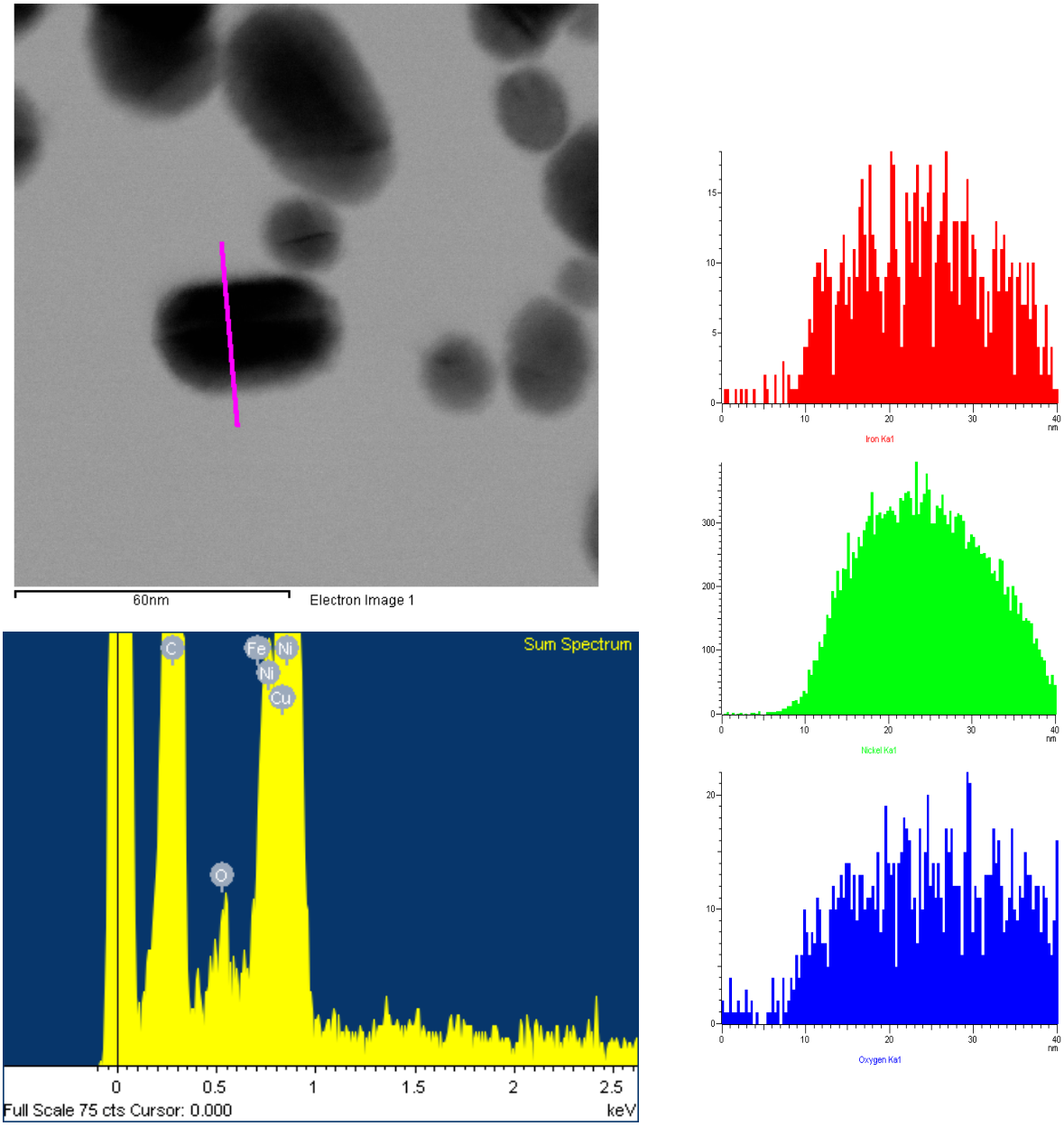

Figure 7-6: EDS of coated nanoparticle. Observe presence of iron (red, top), nickel (green, middle) and oxygen (blue, bottom).

A polycrystalline selected area electron diffraction pattern of a coated particle is shown in Figure 7-7. It is measured and indexed to be nickel and compared with a known pure nickel sample.

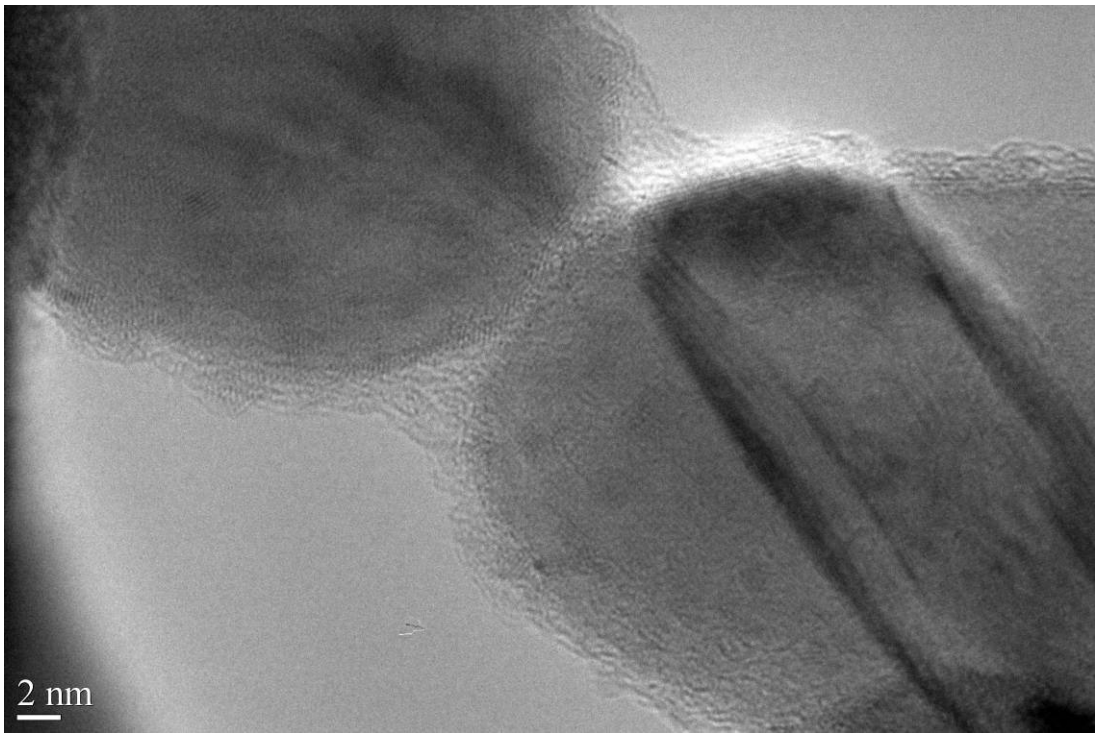

(a)

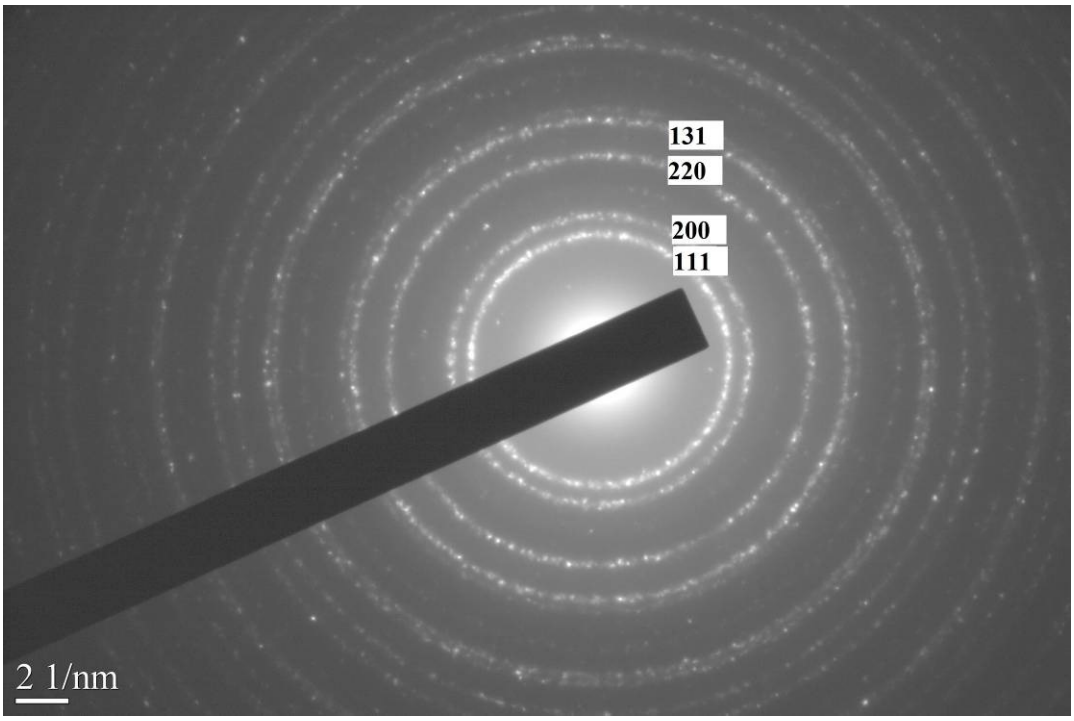

(b)

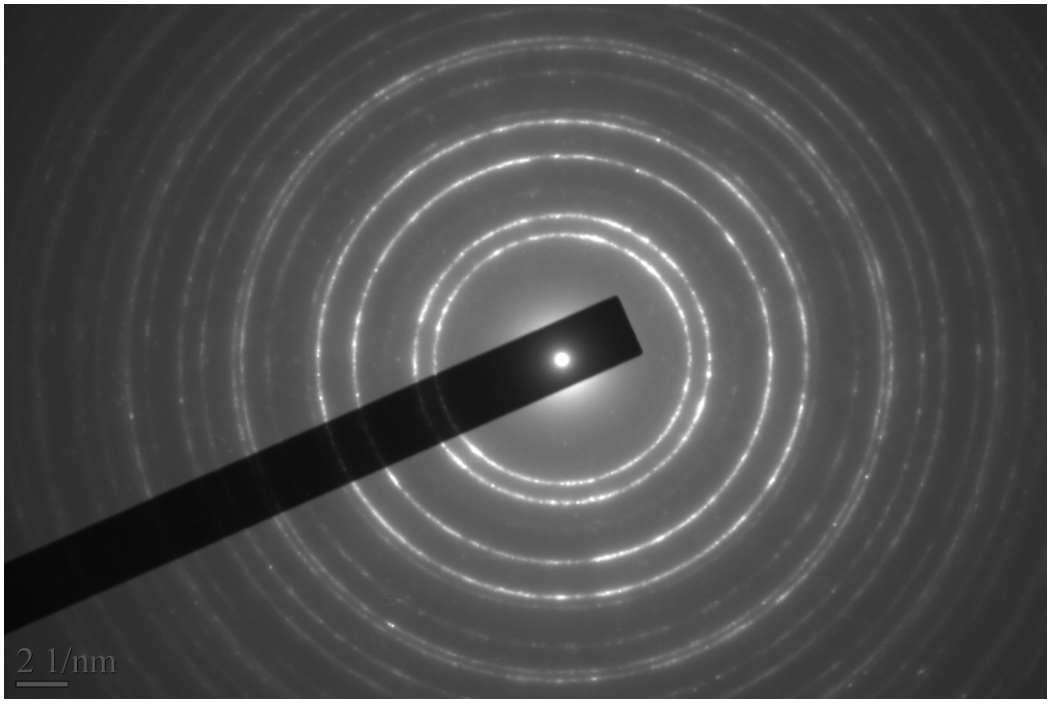

(c)

Figure 7-7: (a) coated nickel nanoparticle examined, (b) indexed polycrystalline electron diffraction pattern of image (a), (c) reference pure nickel polycrystalline electron diffraction pattern.

7.3.3 Excess Iron Oxide Deposits

An interesting feature of the coated agglomerates is that in between two particles, a build up of iron oxide is observed. This phenomenon of oxide build up is described by Phung et al as “hills” of oxide that grow in preferential nucleation sites on the particles surface[75]. We believe that the extreme radius of curvature that occurs in the ‘valley’ of these agglomerations create the preferential growth site for deposition of iron oxide.

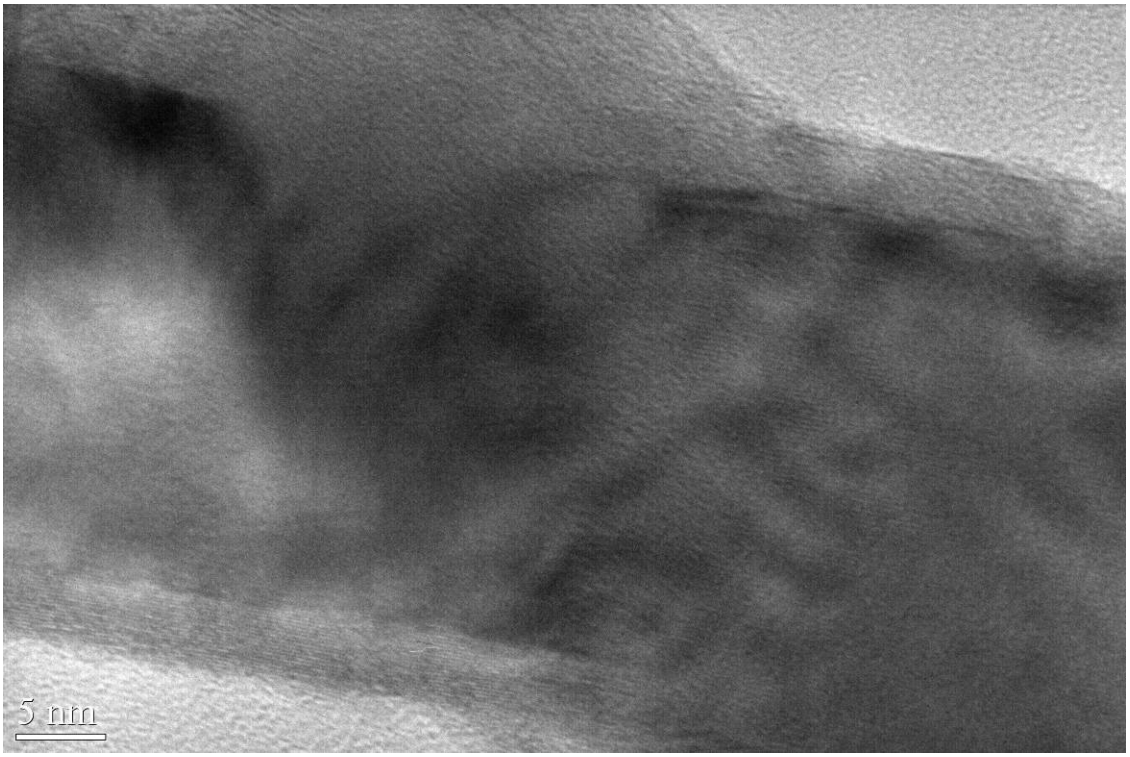

Figure 7-8: TEM image of iron oxide build up in the ‘valley’ between two nickel nanoparticles.

7.4 Cabrera-Mott Theory and the Enlarged Iron Oxide Layer

Cabrera-Mott theory provides growth time for iron oxide layers of 1nm in 0.2fs, 2nm in 40s, and 3nm in 40 weeks at room temperature[13-15; 76]. How than can we see up to 5nm thick shells? Looking at the environment our particles experience reveals two probable sources. Cabrera-Mott theory is based on the electric field created just after the

first oxygen diffuses to iron's surface. It is this e-field that attracts Fe+ ions towards the oxide surface and grows the oxide layer. Exposure to an external electric field increases the depth of oxidation of iron or alternatively, speeds the oxide layer growth. It is thought that the electric field in our DMA and aerosol sampler can enlarge this oxide layer. Another factor that would increase the final oxide layer thickness is the increased temperature of the iron's surface when exposed to air. The aerosol exits the furnace at a temperature of approximately 500ºC. Now if the nanoparticles alone were exposed to room temperature they would cool very quickly, but since they are surrounded by the hot gas it is appropriate to consider the temperature of the aerosol entering the DMA, electrostatic sampler or filter. Ultimately it is believed that when the core-shell particles are exposed to air, it is false to assume they are at room temperature as well.

Empirically, our oxide layer is justified, by Kuhn et al, who observed a 5nm oxide shell on freshly sputtered iron nanoparticles exposed rapidly to ambient air[76; 77]. The thickness of the particles' shell is affected by their collection methods.

7.5 Iron Oxide

The air stable formation of Fe_2O_3, given the abundance of oxygen, is likely the dominant phase and compound on the nickel's surface. The pristine iron is suddenly exposed to air, forming Fe_2O_3 while consuming most of the original iron. Meaning we only add ~3.3nm of iron to nickel, and with oxidation 'swelling' to the observed 5nm of iron oxide. This is an approximate calculation based on the change in densities for Fe and Fe_2O_3. The favorable form of iron oxide is dependent on the temperature at oxidation and level of oxygen present. Likely, our coating is mixture of Fe_2O_3 and Fe_3O_4, but it is hard

to differentiate. Kuhn et al state when the iron nanoparticles are suddenly exposed to air, the shell is formed of "a partially oxidized phase of magnetite (non-stoichiometric Fe_3O_4), while controlled oxidation produce mix of gamma $Fe_2O_3$and Fe_3O_4" [76; 77].

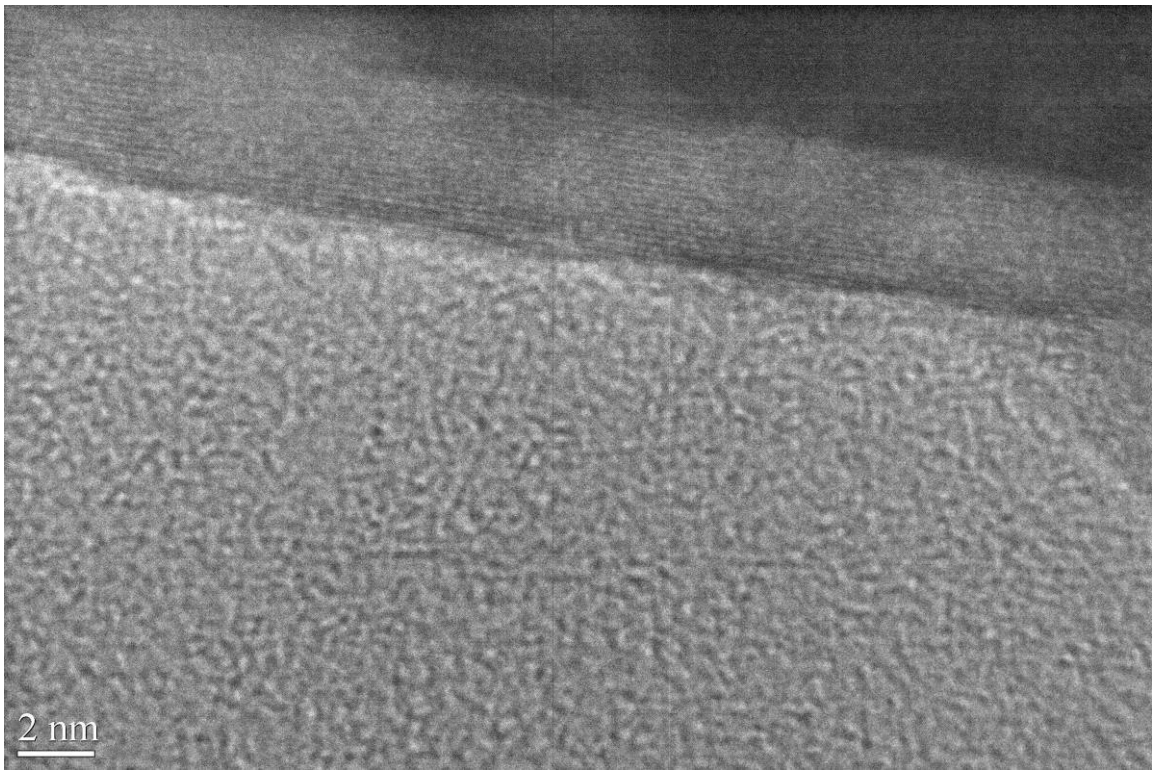

Figure 7-9: HRTEM image of Fe_2O_3 shell

A section of a highly crystalline Fe_2O_3 shell is examined with HRTEM. The individual lattice spacing is very consistent with (222) Fe_2O_3 with a lattice constant 8.33 angstroms. There are 18 oxide layers on the nickels surface providing a theoretical thickness of 4.31nm compared to a measured 4nm. Discrepancies arise mostly from mismatched orientation of Fe_2O_3 (inverse spinel, 8.33 Å) deposited onto Ni (BCC, 3.52 Å) and approximations in measurements. This extreme crystallinity is not observed over the entire shell.

7.6 System Adjustments

In attempt to increase the coating thickness, the evaporation cell is heated to 27ºC and 37ºC. Motivation is that the higher the vapor pressure of iron carbonyl, the higher the concentration of evaporation, and thus more material for the coating. Unfortunately no increase in shell thickness is observed. It possible that either heating the iron carbonyl to this temperature will not significantly increase the actually amount evaporated, or that increased material proceeds to homogenous nucleation and particle growth (thus not adding to the coating thickness). While iron nanoparticles are not observed in TEM and EDS measurements, their existence can not be entirely ruled out; the amount of nickel nanoparticles would greatly outnumber any iron nanoparticles. This requires further exploration, but significant heating of the iron carbonyl is not advised as its decomposition begins at 50ºC.

Chapter 8 Summary and Recommendations for Future Work

Through this investigation we have explored the aerosol generation of aluminum nanoparticles through the precursors triethylaluminum and aluminum trichloride, as well as the synthesis of iron oxide coated nickel nanoparticles. Characterization was conducted using traditional electron microscopy and x-ray energy dispersive spectroscopy. Because our synthesis is gas phase, we were also able to use a scanning mobility particle system to obtain 'on the fly' size distributions that were critical in determining a successful coating.

Using the precursor triethylaluminum, we generated air passivated aluminum nanoparticles combined with a carbon/oxygen based contaminate, which can not be suppressed or eliminated. The system was adapted to the precursor aluminum chloride, in which a silicon contaminate was identified and subsequently eliminated. Ultimately aluminum chloride could not be sufficiently decomposed at temperatures achievable in our tube furnace. Chemical thermodynamic calculations revealed the instability of Al with AlCl, $AlCl_3$ and HCl at high temperatures, and at a decomposition temperature of 1600ºC the favorable formation of AlCl. The study then transitioned to the development of a system to grow an iron oxide shell onto a well characterized nickel nanoparticle aerosol. Through empirical work and calculated decomposition rate, the ideal coating system of iron pentacarbonyl was determined. A successful ~5nm, Fe_2O_3 dominated shell was deposited onto nickel particles and quantified through SMPS and electron microscopy.

Ultimately it would be beneficial to pursue the combination of both themes explored in this research; the synthesis of pristine aluminum and the growth of an iron

oxide coating. This interaction between the aluminum and iron oxide should be investigated to determine its ability to passivate aluminum and whether increased burn rates are observed in comparison to other micron and nano-sized mixed thermites. In the work described here, we only briefly explore control over the iron oxide shell; a more rigorous study is warranted. This is could prove to be a powerful technique, useful in tailoring the stoichiometry of the thermite reaction.

Bibliography

[1] Zhang, L., Ranade, M.B., Gentry, J.W.,. *Aerosol Science* (2004) **35**: pp. 457-471.

[2] Friedlander, S. K.,. Smoke, Dust and Haze. Wiley, New York, 1977.

[3] Hinds, W.,. Aerosol Technology: Properties, Behavior and Measurements of Airborne Particles. Wiley, New York, 1999.

[4] Nasibulin, A.G., Moisala, A., Brown, D. P., Jiang, H., Kauppinen, E. I.,. *Chemical Physics Letters* (2005) **402**: pp. 227-232.

[5] TSI inc. Model 3080-Series Electrostatic Classifier. (2001) .

[6] Cooper, P.W.,. Explosive Engineering. Wiley, New York, 1996.

[7] Cooper, P.W., Kurowski, S.R.,. Introduction to the Technology of Explosives. Wiley, New York, 1996.

[8] Fischer G. 32nd AIAA/ASME/SAE/ASEE Joint Propulsion Conference . (1996) .

[9] Ivanov, G.V. and Tepper, F.,. Fourth International Symposium on Special Topics in Chemical Propulsion. (1997) : p. 636.

[10] Aumann, C.E., Skofronick, G.L., Martin, J.A., *Journal of Vacuum Science & Technology, B: Microelectronics and Nanometer Structures* (1995) **13**: pp. 1178-1183.

[11] Rossi, C., Zhang, K., Esteve, D., Alphonse, P., Tailhades, P., Vahlas, C.,. *J. Microelectromechanical Systems: A Review* (2007) .

[12] Sullivan, K., Young, G., Zachariah, M.R.. Enhanced Reactivity of Nano-B/Al/CuO MIC's, private communication,. (2007) .

[13] Mott, N. F.,. *Trans. Far. Soc.,* (1940) **36**.

[14] Mott, N. F.,. *Trans. Far. Soc.,* (1939) **35**.

[15] Mott, N. F.,. *Trans. Far. Soc.,* (1938) **34**: p. 50.

[16] Dye, R., O'Neill, E., Shelton, D., Walter, K. C.,. *J. Pyrotechnics* (2004) **19**: p. 19.

[17] Park, K., Lee, D., Rai, A., Mukherjee, D., Zachariah, M.R.,. *J. Phys. Chem. B* (2005) **109**: pp. 7290-7299.

[18] Jouet, R.J., Carney, J.R., Granholm, R.H., Sandusky, H. W., Warren, A.D.,. *Materials Science and Technology* (2006) **22**: pp. 422-429.

[19] Jouet, R. J., Warren,A. D., Rosenberg, D. M., Bellitto, V. J., Park, K., Zachariah, M.R.,. *Chemistry of Materials* (2005) **17**: pp. 2987-2996.

[20] Akhavan, J.,. The Chemistry of Explosives. Royal Society of Chemistry, Great Britain., 2004.

[21] Akiba, R., Kohno, M., Volpi, A., Tokudome, S., Shibata, ,T.,. *Combustion, Explosion, and Shock Waves* (1993) **29**.

[22] Kubota N. Propellants and Explosives: Thermochemical Aspects of Combustion. Wile, New York, 2007.

[23] Anno, E., Ymaguchi, T.,. *Surface Science* (1993) **286**.

[24] Jaug, L.Y., Yao, Y.D., Chen, Y.Y, Hwu, Y.,. *Nanostructured Materials* (1997) **9**: p. 531.

[25] Chen, K.Z., Zhang, Z.K., Cui, Z.L., Zuo, D.H., Yang, D.Z.,. *Nanostructured Materials* (1997) **8**: p. 205.

[26] Granqvist,C. G., Buhrma, R. A.. *Journal of Applied Physics* (1976) **47**: p. 2200.

[27] Pfund, A. H.,. . *Phys, Rev. B* (1930) **35**: p. 1434.

[28] Rai, A., Park, K., Zhou, L., Zachariah, M. R.,. *Comb. Theory and Model.* (2006) **10**: pp. 843-859.

[29] Liu, B., Hu, Z., Che, Y., Chen, Y., Pan, X. *Appl. Phys. Lett.* (2007) .

[30] Zhang, B.,. **"Thermal Plasma Synthesis and Photoinduced Coating of Aluminum Nanoparticles**. University of Minnesota.2007.

[31] Masuda, H., Higashitani, K., Yoshida, H.,. Powder Technology Handbook. CRC Press, Florida, 2006.

[32] Okuyama, K., Lenggoro, I. W.,. *Chem. Eng. Sci.* (2003) **58**: pp. 537-547.

[33] Gurav, A., Kodas,T., Pluym, T., XiongY.,. *Aerosol Sci. Technology* (1993) **19**: p. 411.

[34] Kim, J. H., Germner, T.A., Mulholland, G.W., Ehrman, S. H.,. *Adv. Mater.* (2002) **14**.

[35] Kodas, T.T., Hampden-Smith, M.J.. Aerosol Processing of Materials. Wiley, New York, 1999.

[36] Heist, R., Derenthal, J.,. *Lecture Notes in Physics: Atmospheric Aerosols and Nucleation* (1988) **309**.

[37] He, H., Heist, R. H. Mcintyre, B.L, Blanton, T.N.,. *Nanostructured Materials* (1997) **8**.

[38] Glass, J.A., Hwang, S. D., Datta, S., Robertson, B., Spencer, J. T.,. *J. Phys. Chem. Solids* (1996) **57**.

[39] Hitchman, L. M., Jones, A.C., Hitchman, M.L.,. Chemical Vapour Deposition: Precursors and Processes. Royal Society of Chemistry, Great Britian, 2009.

[40] McGrew, C.E.,. Next-generation CVD aluminum precursors pose new handling challenges. *Solid State Technology* (June 1997).

[41] Gladfelter, W.L., Boyd, D.C., Jensen, K.F.,. *Chemistry of Materials* (1989) **1**: pp. 339-343.

[42] Smith, M. B.,. *J. Phys. Chem.,* (1967) **71**: pp. 364-370.

[43] Nakajima, T., Nakatomi, M., Yamashita, K.,. *Molecular Physics* (2003) **101**: pp. 267-276.

[44] Frigo, D.M., van Eijden, G. J. M., Reuvers, Smit, C. J.,. *Chemistry of Materials* (1994) **6**: pp. 190-195.

[45] Bent, B. E., Nuzzo, R. G., Dubois, L. H.,. *J. Am. Chem. Soc.* (1989) **111**: pp. 1634-1644.

[46] Amazawa T.,. *J. Electrochemical Soc.* (1998) **145**.

[47] Tsubouchi, K., Masu, K.,. *J. Vac. Sci. Technol. A* (1992) **10**: p. 856.

[48] Kondoh, E., and Ohta, T.,. *J. Vac. Sci. Technol. A* (1995) **13**: p. 2863.

[49] Boldt, J.R.,. The Winning of Nickel. Methuen Publishing Company, New York, 1967.

[50] Chan RARM. *Canadian Journal of Chemistry* (1962) **40**: pp. 845-855.

[51] Day, J. P., Pearson, R.G., Basolo, F.,. *Nanostructured Materials* (1997) **8**.

[52] Park, J.H., Sudarshan, T. S.,. Chemical Vapor Deposition, Chapter 9, CVD of Metals: A Case for Nickel. ASM Internantional , 2000.

[53] Patnaik, P.,. A Comprehensive Guide to the Hazardous Properties of Chemical Substances. Wiley, New York, 2007.

[54] Brissonneau, L., Reynes, A., Vahlas, C.,. *Chem. Vap. Deposition* (1999) **5**.

[55] Sahnoun, R., Brissonneau, L., Rotaru, C., Mijoule, C., Vahlas, C.,. *Proceedings of the Symposium of Fundamental Gas-Phase and Surface Chemistry of Vapor-Phase Materials Synthesis* (1999) **98**.

[56] Wang, W., Itoh, Y., Lenggoro, I. W., Okuyama, K.,. . *Mat. Sci. and Eng. B,* (2004) **111**: pp. 69-76.

[57] Huber, D.L.,. *Small* (2005) **5**: pp. 482-502.

[58] Tepe, R. K., Jacksier, T., Barnes, R.,. *J. Analytical Atomic Spectrometry* (1998) **13**.

[59] Karlsson, L.S., Deppert, K., Malm, J.O.,. *J. Nanoparticle Research* (2006) **8**: pp. 971-980.

[60] Karlsson, M.N.A., Deppert, K., Wacaser, B.A., Karlsson, L.S., Malm, J.-O.,. *Appl. Phys. A* (2005) **80**: pp. 1579-1583.

[61] Shao, H. P., Lee, H. S., Suh, Y. K., Kim, J. H., Li, Y., Kim, C.O.,. *J. of Iron and Steel Research, International* (2006) : p. 205.

[62] Dumestre, F. Chaudret, B., Amiens, C., Renaud, P., Fejes, P.,. *Science* (2004) **303**: pp. 821-823.

[63] Smith, W.L., Wychick, D.,. *J. Phys. Chem.* (1980) **84**: pp. 1621-1629.

[64] Eriguchi, K., Murakami, H., Panyukova, U., Kumagai, Y., Ohira, S., Koukitu, A.,. *J. of Crystal Growth* (2007) **289**: pp. 332-335.

[65] Heyman, A., Musgrave, C.B.. *J. Phys. Chem. B* (2004) **108**: pp. 5718-5725.

[66] Roesky, H.W., Kumar, S.S.,. *Chem. Comm.* (2005) : pp. 4027-4038.

[67] Catoire, L., Swihart, M.,. *J. of The Electrochem.Soc.* (2002) **149**: p. C261-C267.

[68] Stull, D.,. *Ind. Eng. Chem.* (1947) **39**: p. 540.

[69] Zhou, L., Rai, A., Piekiel, N., Ma, X., Zachariah, M.,. *J. Physical Chemistry C* (2008) **112**: pp. 16209-16218.

[70] Itri, R., Depeyro, J,. Tourinho, F.A., Sousa, M.H.,. *European Physical Journal E* (2001) **4**: pp. 201-208.

[71] Stappert, S., Rellinghaus, B., Acet, M., Wassermann, E. F.,. *Proceedings of Symposiums W of 2001 Fall Meeting: Nanoparticulate Materials* (2001) **704**.

[72] Beav, A.K., Gaidym, I.L., Demyanchuk, V.V.,. *Zh. Fiz. Khim* (1975) **49**: pp. 2575-2577.

[73] Moisala, A., Nasibulin, A. G., Brown, D. P., Jiang, H., Khriachtchev, L., Kauppinen, E.I.,. *Chem. Eng. Sci.,* (2006) **61**.

[74] Biswas, P., Wu, C.Y., Zachariah, M.R., McMillin B.,. *J. Mater. Res.,* (1997) **12**.

[75] Phung, X., Groza, J., Stach, E.A., Williams, L. N., Ritchey, S. B.,. *Materials Sci. and Eng.* (2003) **A 359**: pp. 261-268.

[76] Kuhn, L. T., Bojesen, A., Timmermann, Nielsen, M. M., Morup, S. *Journal of Physics: Condensed Matter* (2002) **14**: pp. 13551-13567.

[77] Kuhn, L. T., Bojesen, A., Timmermann, L., Fauth, K., Goering, E., Johnson, E., Nielsen, M. M., Morup, S.,. *Journal of Magnetism and Magnetic Materials* (2004) **272**: pp. 1485-1486.